

1 **Title**

2 Paleotsunami record of the past 4300 years in the complex coastal lake system of Lake Cucao,
3 Chiloé Island, south central Chile

4 **Authors**

5 Philipp Kempf^{1,2,*}, Jasper Moernaut³, Maarten Van Daele², Mario Pino⁴, Roberto Urrutia⁵, Marc
6 De Batist²

7 *corresponding author: philipp.kempf@fu-berlin.de

8 **Affiliations**

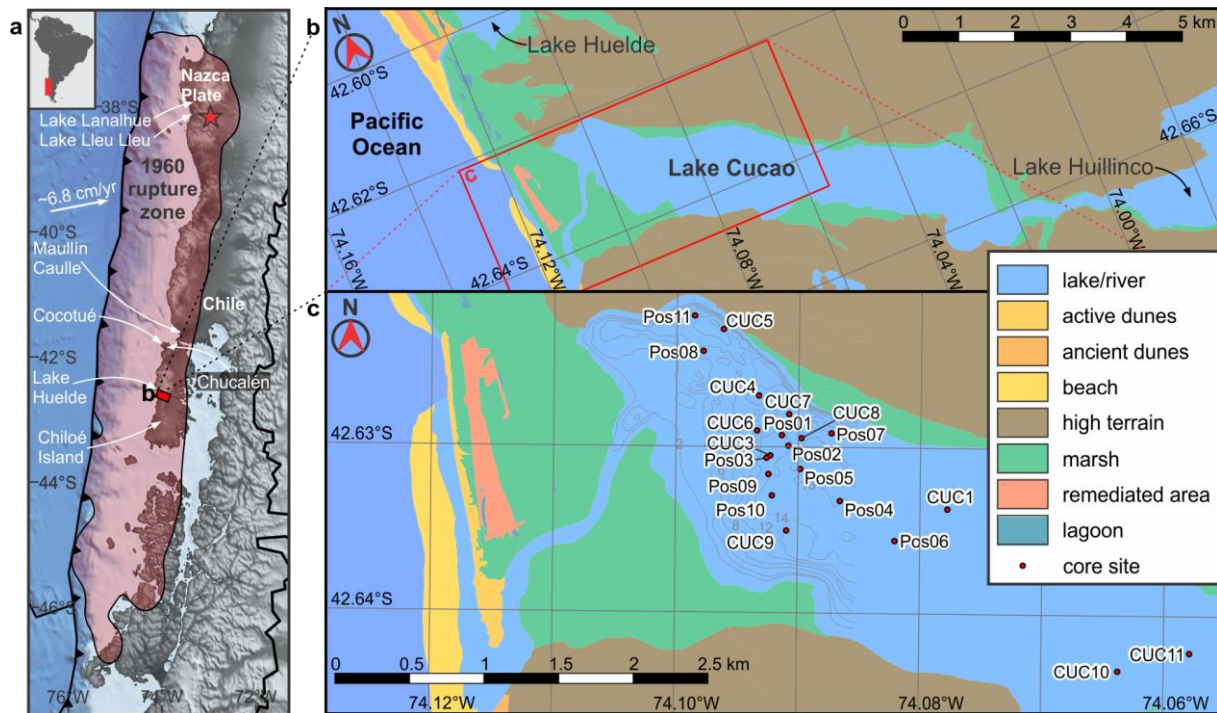
- 9 1) Institute of Geological Sciences, Freie Universität Berlin, Berlin Germany
10 2) Renard Centre of Marine Geology, Ghent University, Gent, Belgium
11 3) Institute of Geology, University of Innsbruck, Innsbruck, Austria
12 4) Instituto de Ciencias de la Tierra, Universidad Austral de Chile, Valdivia, Chile
13 5) Centro EULA Chile, Universidad de Concepción, Concepción, Chile

14 **Abstract**

15 In CE 1960, Lake Cucao on Chiloé Island in south central Chile was inundated by the tsunami
16 of the Great Chilean Earthquake (Mw 9.5). The area of what is now the lake basin has been
17 submerged since the end of the rapid postglacial sea-level rise and has recorded tsunami
18 inundations in its sediment record since then. This study reconstructs the tsunami history of Lake
19 Cucao. Reflection-seismic profiles and side scan sonar data of the lake reveal a tidal delta with a
20 crosscutting channel, which controls the sedimentary environment in the coast-facing part of
21 Lake Cucao. The convergent pattern of seismic reflections near this channel indicates that tidal
22 currents were active in the lake at least episodically since the formation of a major unconformity
23 with strong reflection amplitude, which records the onset of lacustrine sedimentation. A
24 radiocarbon date at the base of one of the 21 collected sediment cores dates this reflector to
25 ~3800 years BP. Little net vertical displacement (≤ 2 m) in combination with an outlet river
26 channel that can act as a pathway for sediment transport appears to have maintained the
27 sensitivity of Lake Cucao to record tsunami inundation. The sedimentary record contains 15
28 clastic layers which are interpreted as tsunami deposits. The confidence level on the tsunami
29 interpretation depends on five site-specific criteria, which are: (i) high magnetic susceptibility of
30 the sediment indicating high clastic content, (ii) cross core correlation indicating widespread
31 deposition, (iii) acoustic reflector correlation to the sedimentary record (also indicating
32 widespread deposition), (iv) presence of mud clasts, and (v) age correlation to known
33 paleotsunamis in the area. In this way, eight clastic layers are interpreted as tsunami deposits
34 with a high confidence level, five with a medium confidence level and two with a relatively low
35 confidence level. This study adds a long paleotsunami record on a coastline where extreme
36 tsunamis occur frequently and where long (>2000 years) paleotsunami records are still sparse.

37 **Keywords**

38 Tsunami deposits, lacustrine sediments, reflection-seismic profiles, south central Chile, coastal
39 sediment dynamics.

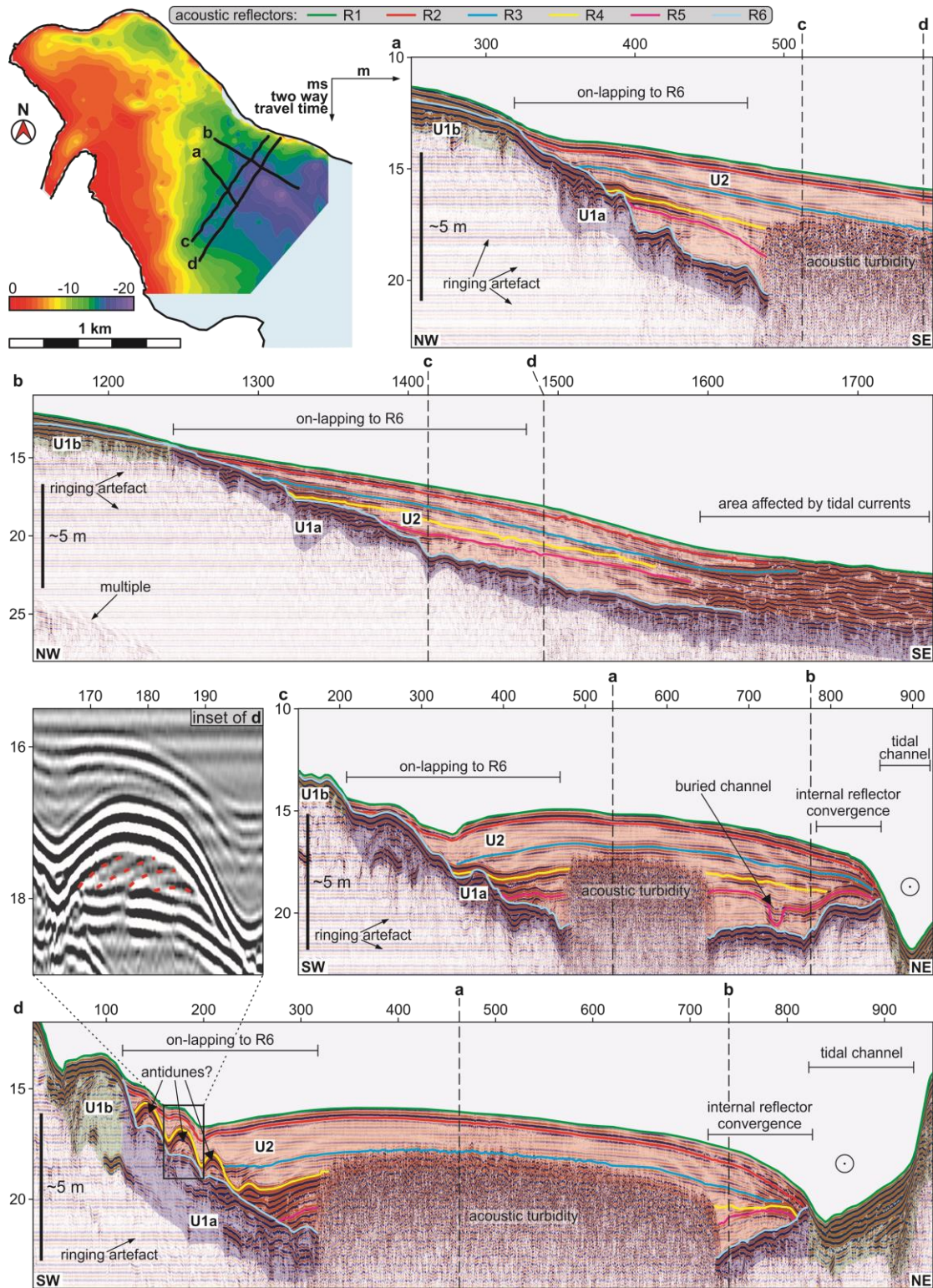


40
41 *Figure 1. (a) Topographic and bathymetric overview of south central Chile. The digital elevation*
42 *model is based on the ETOPO1 dataset (Amante and Eakins, 2009). The epicentre and the*
43 *1 m slip contour line representing the rupture zone (Moreno et al., 2009) of the CE 1960*
44 *earthquake are drawn in red. Locations of coastal sediment records discussed in the text*
45 *are indicated in white; (b) detailed map of the study area. The geomorphological units are*
46 *based on field observations and are extended using satellite imagery (Google Earth). (c)*
47 *The lake bathymetry map is based on side scan sonar bottom tracks (Kempf et al., 2015).*

48 1 Introduction

49 Long and continuous sedimentary records of infrequent large-scale tsunamis are essential in
50 characterising recurrence patterns – a prerequisite for reliable hazard assessments. In recent
51 decades the scientific means to study the sedimentary record of tsunamis has grown in quantity
52 and quality (e.g., Chagué-Goff et al., 2011, 2017). Linking tsunami deposits to documented
53 historical tsunamis is a necessary step to calibrate tools in paleotsunami research (e.g., Costa et
54 al., 2016). However, the primary reason for sedimentological investigations is to extend the
55 historical record which is often not long enough to capture the variability in tsunami recurrence
56 (Kempf et al., 2018). This is a challenging task because long and continuous sedimentary records
57 in often highly dynamic coastal areas are rare.

58 Written history in south central Chile begins with the Spanish invasion in CE 1535 (Lomnitz,
59 1970, 2004; Cisternas et al., 2005). In the ~500 years since then, four major earthquakes were
60 chronicled in the area between the Arauco peninsula (~37°S) and the Chile Triple Junction
61 (~46°S). The latest was the CE 1960 Great Chilean Earthquake (M_w 9.5), notorious for being the
62 strongest earthquake on instrumental record. The older events occurred in CE 1575, 1737 and
63 1837. According to damage reports, tsunamis damaged coastal towns in all but the CE 1737
64 earthquake. Sedimentological investigations produced evidence for tsunami inundation for all
65 four documented tsunamis in many coastal areas of Chile (Cisternas et al., 2005, 2017; Reinhardt



66

67 *Figure 2: Sub-bottom profiles show the seismic stratigraphy of Lake Cucao with seismic units*
 68 *U1a (blue), U1b (green) and U2 (red). Profiles a) and b) parallel to the lake's long axis*
 69 *image the on-lapping of the internal acoustic reflectors R1–R5 onto acoustic reflector R6.*
 70 *Profiles in cross-direction to the lake's long axis c) and d) show down-lapping in the*
 71 *southeast and convergent internal reflectors towards the tidal channel. Reflector R4*
 72 *expresses three hummocks (see inset), which are interpreted as antidunes.*

73 et al., 2010; Atwater et al., 2013; Ely et al., 2014; Dura et al., 2015; Garrett et al., 2015; Kempf
74 et al., 2015; Nentwig et al., 2015). In addition, six sites, Tirúa (Nentwig et al., 2018), Maullín
75 (Cisternas et al., 2005), Caulle (Atwater et al., 2013), Chucalén (Garrett et al., 2015), Cocotué
76 (Cisternas et al., 2017) and Lake Huelde (Kempf et al., 2017) are known to have recorded
77 tsunami inundation before the earliest written reports of earthquake and tsunami damage in CE
78 1562 (Lomnitz, 2004) (Fig. 1). Of these six sites, only the Maullín and Lake Huelde records
79 extend the tsunami history past 1000 years BP, highlighting the need for adequate sites that have
80 a long sedimentary tsunami record.

81 One of the difficulties when investigating tsunami deposits on millennial timescales is relative
82 sea-level change, which plays a key role in tsunami deposition and preservation (Kelsey et al.,
83 2015; Dura et al., 2016, Szczuciński, 2020). Relative sea-level rise creates the needed
84 accommodation for tsunami deposit preservation in coastal lowlands. However, with too much
85 relative sea-level rise or fall, coastal erosion or progradation, the shoreline displacement may
86 shift the area of tsunami deposition with respect to previous tsunami deposits, which makes long
87 and continuous paleotsunami records from coastal lowlands rare. In contrast, coastal lakes can
88 provide excess accommodation and may be in a position with a relatively stable sensitivity to
89 record tsunami inundation since the culmination of the early Holocene sea-level rise.

90 This study partially builds on a chapter in the doctoral thesis of the first author (Kempf, 2016). It
91 presents a long and continuous sedimentary record from coastal Lake Cucao, with multiple
92 tsunami deposits reaching back to ~4300 years BP based on a dense coverage of acoustic data
93 and 21 sediment cores. The quality of the tsunami record is assessed by evaluating the
94 sedimentary environment, tsunami deposit composition and age correlation with paleotsunamis
95 in the region. The spatial multiproxy approach allows us to assign a confidence level to the
96 interpretation as tsunami deposits, allowing a better evaluation of the temporal correlation of
97 paleotsunamis.

98 **2 Setting**

99 Lake Cucao (74.09°W, 42.63°S) is a coastal lake located on the west coast of Chiloé Island in
100 south central Chile (Fig. 1a). It is connected to the Pacific Ocean by its outlet river channel,
101 which crosses the 1.3 km wide barrier of an up to 250 m wide beach, a narrow belt of active
102 dunes followed by ancient dunes and pastures (Fig. 1b). Lake Cucao is an elongated lake with its
103 long axis in NW-SE direction of 7.9 km and a width of ~1.5 km. It is 10.6 km² in size and up to
104 25 m deep. It has a small catchment to lake surface ratio of 3.1:1, because of the upstream
105 adjacent Lake Huillinco. The only direct riverine input is a small creek from the south in the
106 eastern part. The outlet channel of the lake facilitates water exchange between lake and ocean in
107 both directions, because the lake level lies in the intertidal zone (Villalobos et al., 2003; Kempf
108 et al., 2015). The closest monitored tide gauges in the port of Ancud, 90 km to the north on
109 Chiloé Island, record diurnal micro- to mesotidal (0.0 to 4.1 m tidal range between neap and
110 spring tides) regime. The exchange of water forms a stable saline bottom water layer in Lake
111 Cucao (10.4 ‰) and Lake Huillinco (18.9 ‰) (Villalobos et al., 2003) (Fig. 1). With the
112 transport of water from the Pacific comes erosion, transport and deposition of sediment, which
113 produced a tidal delta around the outlet channel in Lake Cucao. Active mega-ripples on the tidal

114 delta and a crosscutting channel through the delta are the bedform expressions of present-day
115 tidal currents (Kempf et al., 2015) (Figs. 2, 3).

116 **3 Methods**

117 **3.1 Hydroacoustic surveys**

118 The complex sedimentary system around Lake Cucao's outlet, was imaged with a Klein3000
119 side scan sonar, which uses 100 kHz and 500 kHz frequencies to produce a 50 m wide swath of
120 the lake floor's acoustic reflectivity. The data were visualised with SonarWizMap v4 and has
121 been presented in detail in Kempf et al. (2015). Here, we make use of the mapped active mega-
122 ripple crest outlines to show the pattern of active currents (Fig. 3).

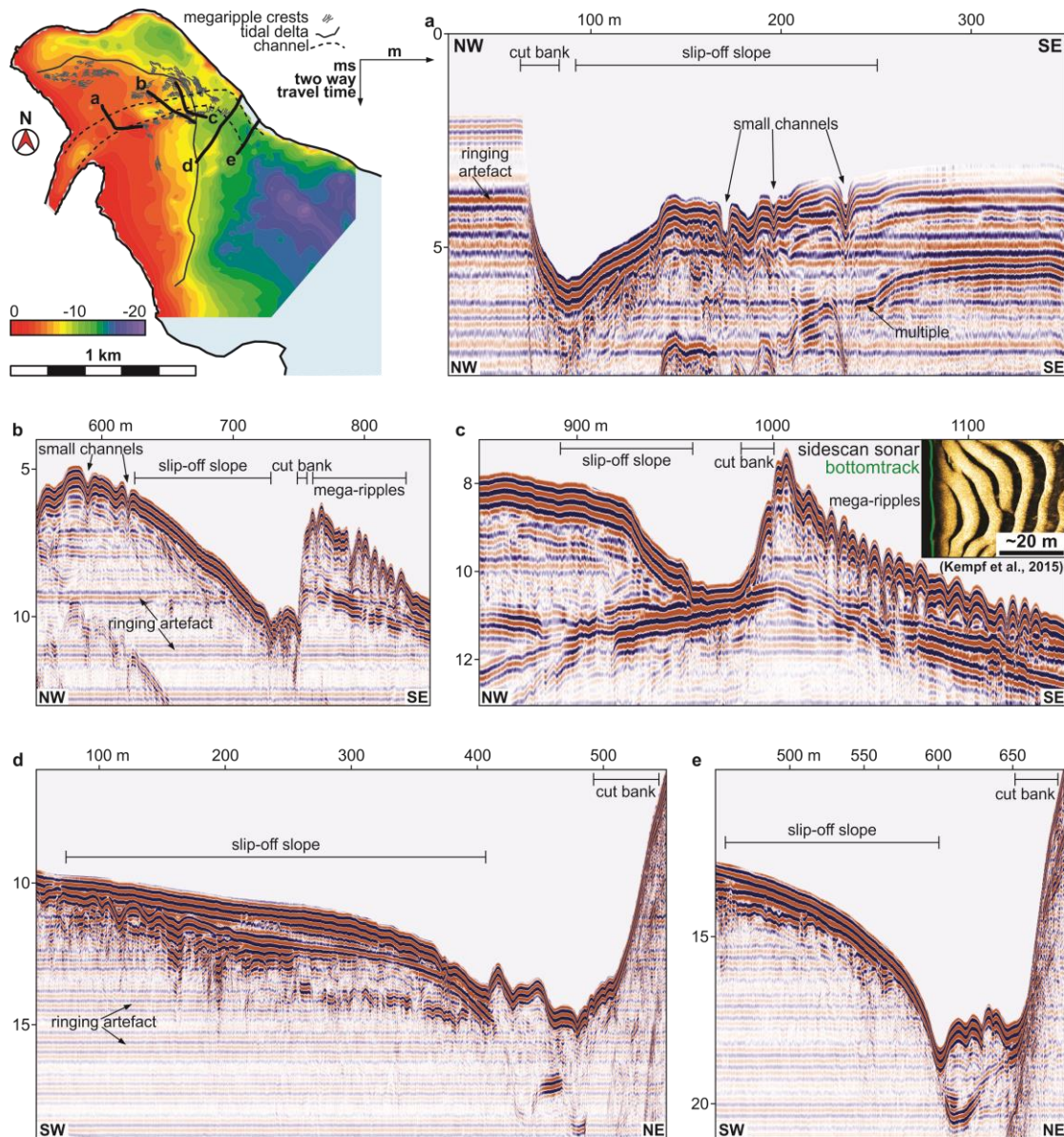
123 We collected 25 km of high-resolution reflection-seismic profiles with a 3.5 kHz GeoAcoustics
124 GeoPulse pinger in 71 lines. At 3.5 kHz, the vertical resolution is between 10 and 20 cm. The
125 data were visualised and interpreted with IHS Markit Kingdom v8.8. We use the reflection-
126 seismic profiles (i) to image the sedimentary architecture of the lake basin infill, (ii) to map
127 geomorphologic features, (iii) to describe the general seismic stratigraphy, (iv) to determine
128 coring sites, and (v) to integrate the sediments cores with acoustic data (ground truthing)

129 **3.1 Sediment core analysis**

130 In total, we cored at 21 locations in Lake Cucao, 9 of which were cored deeper than 2 m burial
131 depth, i.e., depth below lake floor surface in sediment cores, with a maximum of ~8 m burial
132 depth recovered. The top core section at each coring site is comprised of a gravity core, because
133 gravity corers produce relatively undisturbed near-surface sediment samples. Any deeper core
134 sections were obtained with a UWITEC hammer-driven piston corer. Deep and full recovery was
135 achieved by overlapping 3-m-long core sections to produce composite cores. Both types of cores
136 have a 6 cm inner diameter.

137 Each split core was analysed with a multi-sensor core logger (Geotek MSCL) for high-resolution
138 line scan core surface imagery, gamma ray attenuation density logging and magnetic
139 susceptibility logging (Bartington MS2E point sensor with a 3.8 mm area of response in z-
140 direction) at 2 mm increments. The organic content of organic-rich mud was estimated using
141 protocols in Heiri et al. (2001) for loss on ignition to 550 °C (n=8). Some core sections were X-
142 ray CT-scanned with a Siemens Flash medical CT-scanner with a voxel size of ~0.15×~0.15×0.6
143 mm. Grain size distributions were measured at the base of five cores (n=7) with a Malvern
144 Mastersizer 2000 after treatment with 2 ml of 35% hydrogen peroxide to dissolve organic
145 content (where necessary this step was repeated), 1 ml of 10% nitric acid to dissolve calcareous
146 content and 300 mg sodium hexametaphosphate to prevent grain flocculation. Material for
147 radiocarbon dating was extracted by either identifying macrofossils or by wet-sieving 1 cm thick
148 slices of sediment and picking remains of plants and periostraca in the sieve (Table 1).

149 The age control is based on seven radiocarbon dates (Table 1) and the results of Kempf et al.
150 (2015), who identified the youngest clastic layer as the CE 1960 tsunami deposit by the means of
151 ¹³⁷Cs and ²¹⁰Pb-dating. The radiocarbon dates were calibrated using the southern hemisphere
152 calibration curve SHCal13 (Hogg et al., 2013). The samples are comprised of leaves, small plant
153 fragments and periostraca of (probably) *Diplodon chilensis* and fragments thereof. *Diplodon*
154 *chilensis* is a freshwater clam species (Valdovinos and Pedreros, 2007).



155
 156 *Figure 3: Sub-bottom profiles across the tidal channel expressing the asymmetry of the channel*
 157 *with alternating slip-off slopes and cut banks. Tidal currents produce mega-ripples outside*
 158 *the cut bank and small channels are present on the upper bank of the slip-off slope.*

159 **4 Results**

160 **4.1 Seismic stratigraphy**

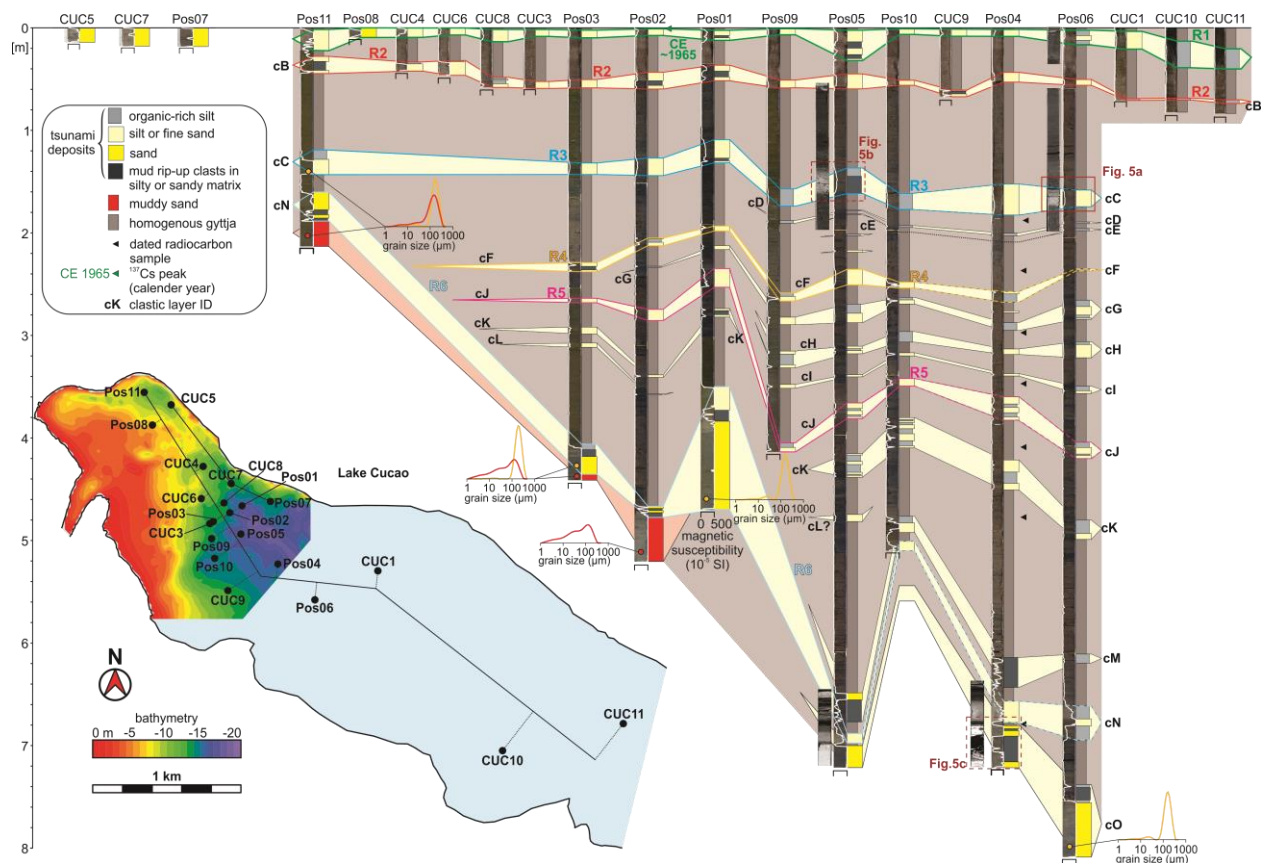
161 Two seismostratigraphic units can be differentiated on reflection-seismic data from Lake Cucao,
 162 U1 and U2 (Kempf et al., 2015). U1 (a and b) includes the acoustic base of the sedimentary
 163 infill. Acoustic penetration into this unit is limited to 1 to 2 m in most places. In few windows
 164 the acoustic signal returns from up to 5 m below U1's top. U1a and U1b are two sub-units of U1
 165 that laterally merge into one another. U1a is covered by the lake's sedimentary infill in relatively
 166 deep areas, whereas U1b is at least sporadically reworked (Fig. 2). The paleo-surface of the top
 167 of U1 is defined by a hummocky surface, which is always a high-amplitude reflection. The
 168 amplitude of reflections below the top decreases quickly in most places. High frequency, high-
 169 amplitude continuous and discontinuous internal reflections dominate in U1.

170 *Table 1. Radiocarbon data for fossil leaves, plant fragments and periostraca from composite*
 171 *core Pos04, which is used as the master core for the age-control of the Lake Cucao*
 172 *sedimentary record.*

sample ID	core ID	section depth	core depth in event-free age model	material	lab ID	¹⁴ C-age	14C-age error	calibrated 95% probability ranges (min., max.)		relative probability	reported ages
								¹⁴ C years BP	years		
CUCA10B-1.5	CUCA10B	1.5	142.5	shell fragment and plant fragments	UBA-37365	26178	161	29970	30867	95	30420 ± 450
CUCA10B-51	CUCA10B	51	190	plant fragments	UBA-37369	5189	56	5756	5823	8.4	5970 ± 210
								5881	6030	73.4	
								6040	6072	2.9	
								6076	6119	6.5	
								6149	6177	3.8	
CUCA11A-52	CUCA11A	52	246	plant fragments	UBA37370	2360	63	2183	2235	4.1	2440 ± 260
								2306	2543	72.9	
								2559	2618	6.2	
								2631	2702	11.7	
CUCA11A-101.5	CUCA11A	101.5	285.5	plant and periostracum fragments	UBA-37368	2166	34	2061	2091	5.7	2180 ± 80
								2097	2212	45.6	
								2220	2308	43.6	
CUCA11B-22	CUCA11B	22	313	plant fragments	UBA-37367	2342	33	2314	2462	95	2390 ± 70
CUCA11B-91.5	CUCA11B	91.5	353.5	periostracum	UBA-37364	2829	38	2852	3034	93	2960 ± 100
								3046	3058	2	
CUCA12B-82.5	CUCA12B	82.5	504	leaf	UBA-21476	3445	34	3617	3621	0.8	3720 ± 110
								3632	3828	94.1	

173
 174 U2 is the lacustrine sediment infill. The basal contact of U2 to U1a creates an unconformity
 175 (reflector R6) characterized by onlapping reflection terminations towards the west. U2 is up to 8
 176 m thick in areas unaffected by acoustic blanking, thinning westward. The internal reflector
 177 geometry of U2 in the upper part (above reflector R4) is parallel to sub-parallel with a low-
 178 amplitude acoustic facies including infrequent high-amplitude, continuous reflections. (Fig. 2c).
 179 The lower part of U2 (below reflector R4) represents a more complex infill pattern with few
 180 internal unconformities. Towards the northeastern shore of the lake U2 gradually transitions
 181 from infrequent parallel to sub-parallel internal reflections to frequent, sub-parallel to hummocky
 182 high-amplitude reflections.

183 The presence of shallow gas in the sediment of the central basin causes acoustic blanking, which
 184 masks the internal reflector geometry of U2 at depths greater than ~1.5 m (2 ms two-way-travel
 185 time, TWT). In total, five parallel to sub-parallel reflectors (R1–R5) can be traced within U2. R1
 186 represents the lake floor and produces a continuous, strong reflection with decreasing amplitude
 187 towards the deeper lake basin in the southeast (Fig. 2). R2–R5 show high-amplitude, continuous
 188 internal reflections and form onlaps to either R6 or to one of the other internal reflectors, e.g., R4
 189 onlaps to R5 in some areas. Of all internal reflectors, R4 has the highest reflection amplitude and
 190 marks the top of a hummocky paleo-surface in the south of the surveyed area (Fig. 2d). The
 191 hummocks are ~30 m long and ~1 m high with up-slope dipping internal reflections. The two
 192 lowermost internal reflectors, R4 and R5, exhibit erosion of the underlying acoustically
 193 transparent lake sediment in the form of buried channels (Fig. 2c).



194
 195 *Figure 4: Core to core correlation of clastic layers in the organic-rich mud-dominated lake*
 196 *sediments. Cores are represented by a split core surface image, a sedimentological core*
 197 *log and in some cases 2D slices of CT-scans. The overview map shows two core transects*
 198 *through the lake. Cores CUC5, CUC7 and Pos07 are located in areas strongly affected by*
 199 *tidal currents. The white line on the split core surface images represents magnetic*
 200 *susceptibility. Grain size distributions are shown in 7 different positions to differentiate*
 201 *muddy sand of tidal delta foresets (red lines) from clastic layers (orange lines). Strong*
 202 *acoustic reflectors are drawn in the same colour as they are on sub-bottom profiles. The*
 203 *seismic to core correlation is captured in figure 6.*

204 **4.2 Lacustrine sedimentary environment and sedimentation**

205 The tidal channel incises the shallow delta up to 3.5 m deep and ~100 m wide, at its western end
 206 as a prolongation of the outlet river channel (Fig. 3a). The bathymetric cross-profiles of the
 207 channel are asymmetric with a flatter slip-off slope and a steeper cut bank of the channel (Fig.
 208 3). The asymmetry changes along the channel. About 10 m wide and 0.5 m deep incised
 209 channels are common on the upper slip-off slope. Mega-ripples with ~8 m ripple wavelength and
 210 ~0.4 m ripple height are abundant around the incised channel, with crests oriented sub-
 211 perpendicular to the channel (Kempf et al., 2015). The channel continues towards the
 212 northeastern shore (Fig. 3b, c) and bends south-eastward to align with the long axis of the lake
 213 from where it continues parallel to the northeastern shoreline (Fig. 3d, e). Towards the channel,
 214 the parallel to sub-parallel sedimentary infill of U2 (R1–R5) becomes convergent (Fig. 2c, d).
 215 On the intertidal delta and in the crosscutting channel, i.e., areas where the top of U1b is at the
 216 lake floor, the sediment consists of a well-sorted medium to fine sand with mostly quartz,

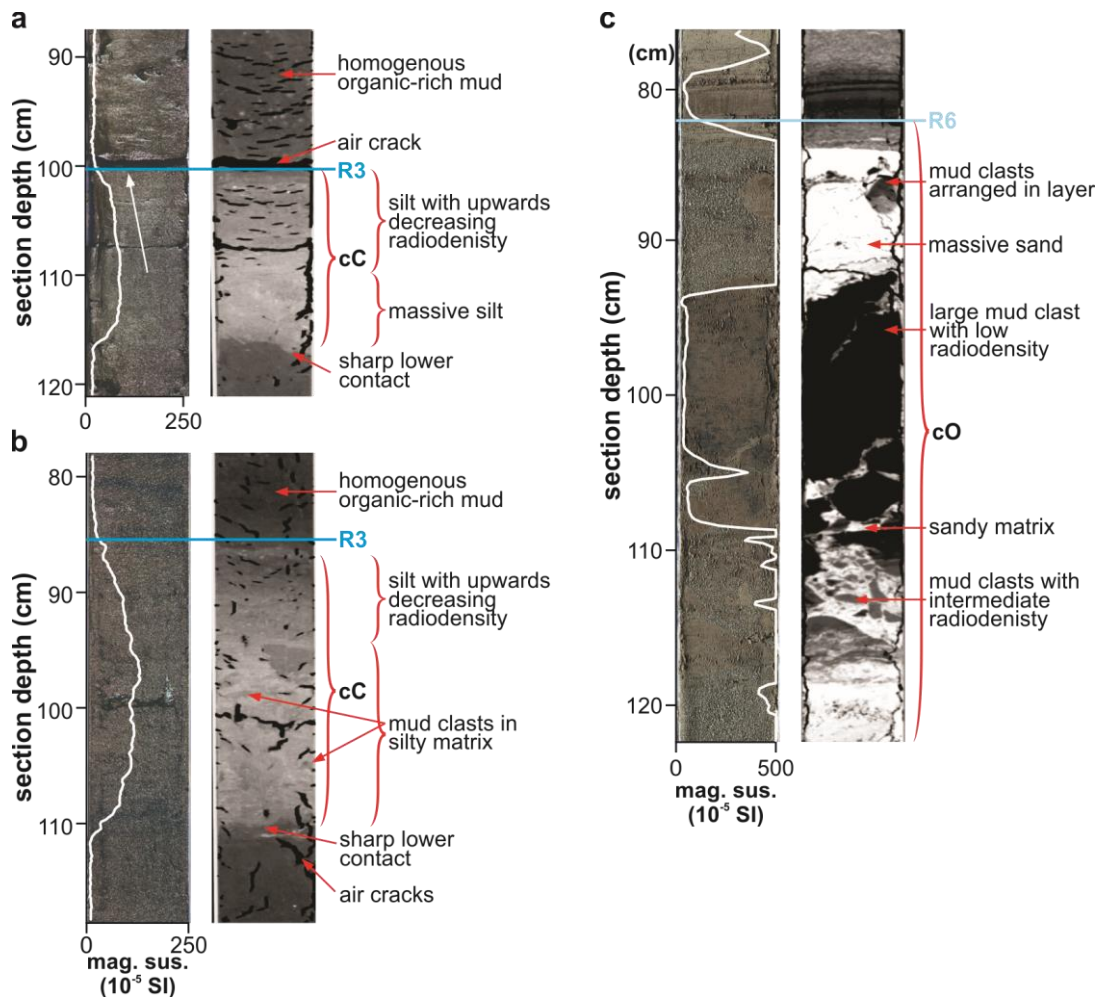
217 feldspar, hornblende and mica minerals (Fig. 4, e.g., core CUC7). The coarse and moderately to
218 well sorted sand prevented penetration deeper than 20 cm with the coring equipment in these
219 locations. This sand is mostly massive with some occurrences of 1 cm thick grey muddy layers.
220 The magnetic susceptibility of this sand is very high, sometimes exceeding 1000×10^{-5} SI.

221 Sediment cores from the lake basin mostly contain brown to black homogeneous, poorly sorted
222 organic-rich mud. The transition from black to brown mud can be gradual or sharp. In the case of
223 sharp transitions, the brown mud is on top. The organic content for both black and brown
224 organic-rich mud is between 20 and 35 weight% (mean = 29.03 weight%, standard deviation =
225 4.18 weight%). The organic matter consists of seeds, fibrous plant material, pollen and
226 fragments of bivalve periostraca without the calcareous shell. The periostraca are sometimes
227 fully preserved with distinct growth rings and are probably from *Diplodon chilensis*, the most
228 common freshwater clam in southern and south central Chile (Valdovinos and Pedreros, 2007).
229 The organic-rich mud smells strongly of hydrogen sulphide when cores are opened the first time
230 (both during fieldwork and in the lab), indicating hypoxic or anoxic conditions. The magnetic
231 susceptibility is low between 0 and 40×10^{-5} SI (Figs. 4, 5).

232 In all 9 long cores, there are 1 to 30 cm thick layers with high clastic components content (Fig.
233 4). The clastic layers are labelled from cA to cO, where “c” stands for Lake Cucao and prevents
234 confusion when correlating to regional records. The capital letter is in alphabetical order down
235 core (Table 2). This is in analogy to similar layers A to H in Maullín (Cisternas et al., 2005) and
236 layers hA to hQ in Lake Huelde (Kempf et al., 2017) (Fig. 1). The topmost clastic layer in Lake
237 Cucao was identified in Kempf et al. (2015) as the tsunami deposit of the CE 1960 tsunami and
238 will be called CE 1960, instead of cA.

239 The clastic layers contain medium silt to fine sand that is coarser than the clastic fraction of the
240 organic-rich mud below and above. However, the clastic layers always contain a fraction of
241 organic matter, too (Fig. 5). The magnetic susceptibility signal of these layers ranges from
242 relatively low, with values between 40 and 100×10^{-5} SI, to relatively high, with values up to
243 500×10^{-5} SI and higher (Figs. 4, 5). The clastic layers are often visually indistinguishable from
244 the organic-rich mud on the split core surface, except for black to brown colour contrasts. CT-
245 scans of the clastic layers reveal sharp lower contacts with the highest radiodensity at the base,
246 gradually decreasing upwards (Fig. 5a, b). Some clastic layers bear 1 to 3 cm diameter mud
247 clasts in a matrix of sand or silt. The mud clasts have lower radiodensity than the matrix and are
248 discernible on CT-scan as darker bodies (Fig. 5b). The mud clasts were difficult to identify on
249 split core surfaces except for clastic layer cN. All other mud clasts were identified on X-ray CT-
250 scans only. If the clastic layers are brown, they often coincide with a sharp colour transition from
251 black to brown at their base. Some clastic layers have recognisable characteristics, e.g.,
252 thickness, colour, shape of the magnetic susceptibility log etc. that can be traced laterally
253 throughout the basin. This way the easiest-to-trace clastic layers were correlated, helping with
254 the correlation of the other clastic layers.

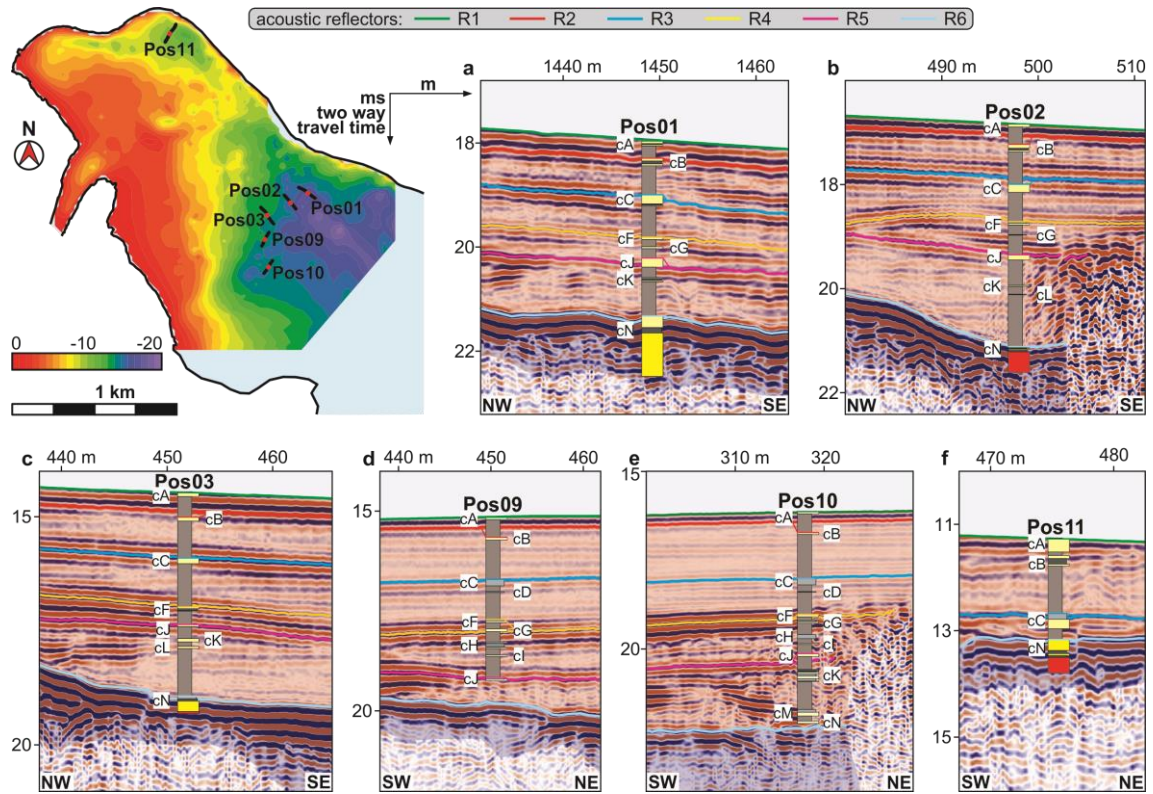
255 Seven of 9 long cores contain the clastic layer cN in the lowest part of the sedimentary record,
256 which appears markedly coarser (fine to medium sand) and exhibits higher magnetic
257 susceptibility values than the other clastic layers, with peaks up to 2500×10^{-5} SI. As in all other
258 clastic layers, the up to 86 cm thick sand of cN does not appear to contain mica. The apparent



259
 260 *Figure 5: X-ray CT-scans of selected core sections. Lighter grey means higher radiodensity. a)*
 261 *and b) CT-scans of clastic layer cC associated acoustic reflector R3; c) clastic layer cN*
 262 *under acoustic reflector R6. All clastic layers exhibit a sharp contact at the bottom. CT-*
 263 *scans in a) and b) show upwards decreasing radiodensity. In b) and c) mud clasts with two*
 264 *differing CT-densities are surrounded by silty (b) to sandy (c) matrix.*

265 lack of mica distinguishes the sand of the clastic layers from the sand in samples from the tidal
 266 delta and the crosscutting channel (Kempf et al., 2015). In layer cN, intervals of well-sorted
 267 massive sands are intercalated with intervals of mud clasts in a sandy matrix. The mud clasts can
 268 exceed the size of the core liner (6 cm) and are up to 11 cm thick (in z-direction). Smaller (< 2
 269 cm) mud clasts are often deposited in thin layers (Fig. 5c). Based on the radiodensity of the mud
 270 clasts, two types can be differentiated; one type with a low radiodensity (black) and a second
 271 type with an intermediate radiodensity (dark grey) (Fig. 5c). The sand of the matrix between
 272 mud rip-up clasts and in intervals of massive sand contain grains of orthoclase, plagioclase,
 273 quartz, iron oxides (responsible for the high magnetic susceptibility), hornblende and rarely
 274 zircon, as well as lithic grains. The same composition of sand is reported for the CE 1960 deposit
 275 in Lake Cucao and Lake Huelde and for the beach sand and dunes sand between Lake Cucao and
 276 the Pacific Ocean (Kempf et al., 2015).

277 Three cores (Pos02, Pos03 and Pos11) contain poorly sorted, muddy sand at their base (Fig. 4).
 278 The mud content makes this sand distinctly different in grain size from the well-sorted sand in
 279 the coarser clastic layers, e.g., clastic layers cC and cN.



280
 281 *Figure 6: Seismic to core correlation of the CE 1960 tsunami deposit (cA) and clastic layers cB*
 282 *to cN (cO not represented on this figure) with strong acoustic reflectors R1 to R6. The*
 283 *assumption of uniform p-wave velocity within the entire lake infill and the piston coring*
 284 *process can cause minor offsets between cores and acoustic reflectors on sub-bottom*
 285 *profiles.*

286 *Table 2: Summary of confidence levels for the interpretation of tsunami deposits for each clastic*
 287 *layer in Lake Cucao, with age and age-correlation to a known tsunami, maximum magnetic*
 288 *susceptibility, traceability of the clastic layers throughout the sedimentary record,*
 289 *correlation to acoustic reflections and content of mud rip-up clasts.*

event name	median age (95% age interval)	potential age-correlation to published tsunami deposits	max. magnetic susceptibility	traceability in the sedimentary record	correlated to acoustic reflector	mud rip-up clasts	confidence level
	cal. years BP		(10 ⁻⁵ SI)	represented in cores/cores reaching this depth interval			
cA/CE 1960	-7 (-11 to -5)	yes	677	18/18	R1	yes	high
cB	287 (185 - 418)	yes	695	17/17	R2	yes	high
cC	1081 (894 - 1274)	maybe	1601	09-Sep	R3	yes	high
cD	1226 (1031 - 1418)	yes	57	05-Aug	-	not observed	medium
cE	1274 (1079 - 1466)	maybe	51	02-Aug	-	not observed	low
cF	1656 (1454 - 1832)	yes	581	08-Aug	R4	yes	high
cG	1825 (1624 - 1986)	yes	431	07-Aug	-	not observed	medium
cH	1962 (1765 - 2109)	yes	202	05-Aug	-	not observed	medium
cl	2099 (1914 - 2213)	no	335	05-Aug	-	not observed	medium
cj	2254 (2077 - 2322)	yes	306	08-Aug	R5	yes	high
ck	2530 (2378 - 2662)	yes	377	07-Jul	-	yes	high
cl	2883 (2670 - 3001)	no	92	03-Jul	-	not observed	low
cM	3699 (3530 - 3906)	yes	585	04-Apr	-	yes	high
cN	3783 (3612 - 3994)	yes	2269	08-Aug	R6	yes	high
cO (in model)	3798 (3626 - 4011)	no	1656	03-Mar	-	not observed	medium
cO (corrected)	4101 (3959 - 4344)	"	"	"	"	"	"

291 **4.3 Correlation between reflection-seismic profiles and sediment cores**

292 Six of the long cores were projected perpendicularly on reflection-seismic profiles that show
293 acoustic penetration of the entire seismic unit U2 (Fig. 6). The correlation between cores and the
294 reflection-seismic profiles is performed under the assumption of a constant p-wave velocity in
295 the entire sedimentary sequence, and no vertical deformation during hammer-driven piston
296 coring, and then tying key marker layer with the reflection-seismic profile. Realistically,
297 variability in p-wave velocity is expected to produce minor offsets. The vertical deformation
298 during hammer coring will cause net compression and wave action on the lake while coring can
299 cause extension, which will likely be heterogeneous and may produce significantly larger offsets.
300 Some offsets are indicated on the reflection-seismic profiles to core correlation (Fig. 6).

301 The six reflectors of U2 (R1 to R6) can all be confidently correlated to clastic layers in the cores
302 (Fig. 4). The top of the CE 1960 tsunami deposit is buried by ≤ 3 cm of lacustrine sediment in
303 the western part of Lake Cucao (Kempf et al., 2015), which is below the vertical resolution of
304 the reflection-seismic profiles. R1, the uppermost strong reflector therefore correlates to the lake
305 floor as well as the top of the CE 1960 tsunami deposit (Fig. 4). R2 correlates to clastic layer cB.
306 However, R2 is so close to the lake floor and R1 reflection, that interference of reflections may
307 lead to a poor identification of R2 in most cases. R3 correlates to cC, R4 to cF, and R5 to cJ,
308 which are major traceable clastic layers in the sedimentary record of Lake Cucao (Fig. 4). Clastic
309 layers with associated reflections (R1 to R6) tend to be especially thick and are represented in
310 most or all cores containing that specific stratigraphic interval (Fig. 4). R6 is the most prominent
311 reflector, because reflectors R2 to R5 onlap to it. Even though onlapping is difficult to observe
312 by comparison of multiple cores, clastic layers cF to cM appear to onlap to cN (Fig. 4). Because
313 of its stratigraphic position, the onlapping and the strong sedimentary contrast between organic-
314 rich mud and the medium sand of clastic layer cN, we correlate the high-amplitude reflector R6
315 to the coarse clastic layer cN (Table 2).

316 **4.4 Age control**

317 The clastic layers exhibit characteristics of abrupt deposition, e.g., sharp lower contacts, mud
318 clasts and radiodensity that decreases upwards, and commonly fining upwards (cf., Van Daele et
319 al., 2014). The intervals of the clastic layers are therefore likely to have been deposited with a
320 different accumulation rate from the rest of the sedimentary record, most likely quasi-
321 instantaneously.

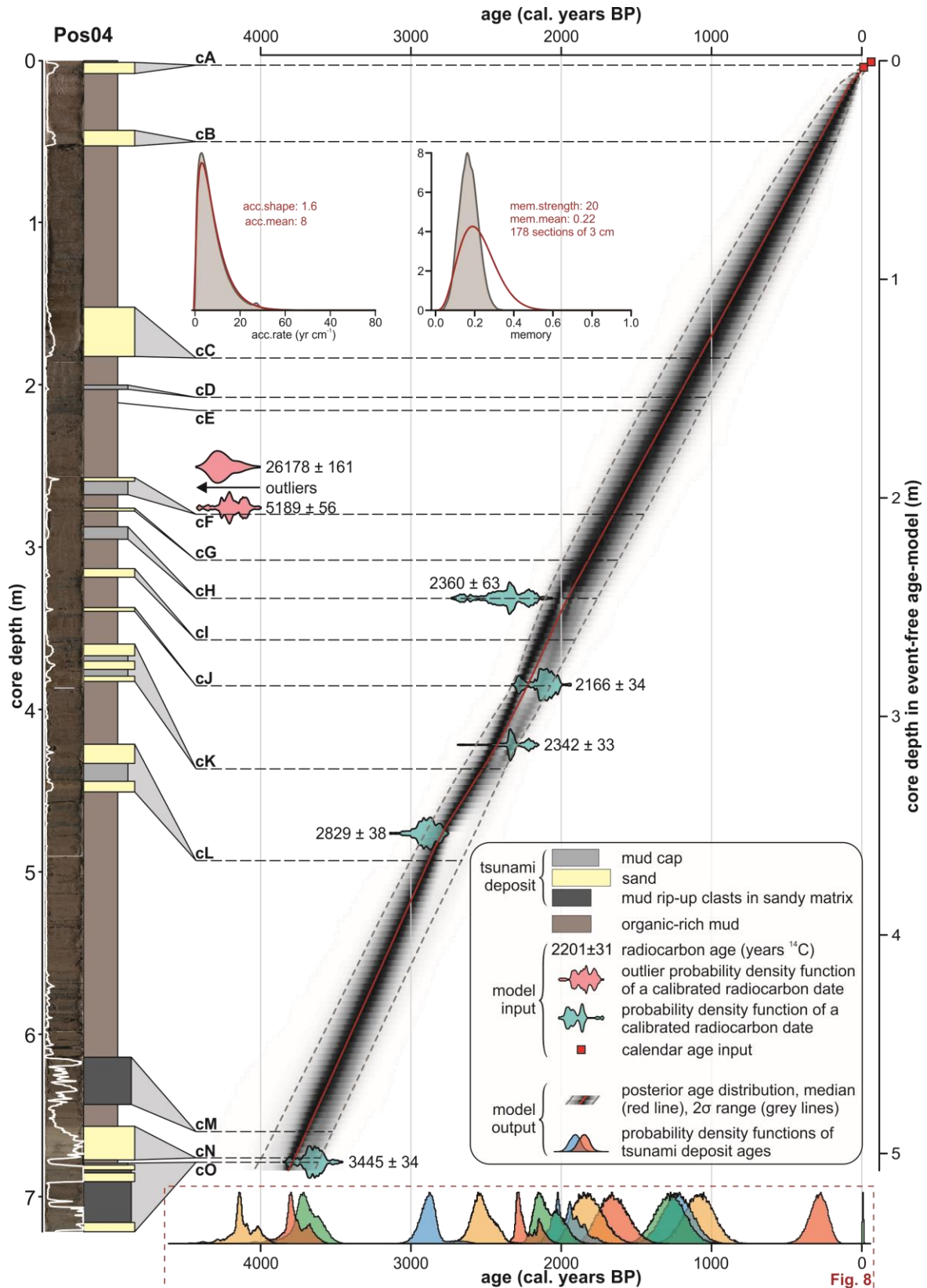
322 We used composite core Pos04 to develop an age-depth model for Lake Cucao. The prior age-
323 depth information consists of the following data and considerations:

- 324 (i) radionuclide data that identified the CE 1960 tsunami deposit (Kempf et al., 2015);
325 (ii) seven radiocarbon dates (Table 1);
326 (iii) clastic layers were treated as instantaneous deposits, i.e., they were taken out of the
327 core for age-depth modelling; and
328 (iv) the sediment is a lacustrine sedimentary sequence, so we assume a relatively stable
329 sedimentation. This is supported by the uniform nature of the sediment sequence with
330 parallel reflections on reflection-seismic profiles at the core site.

331 All age-depth information of Pos04 was fed into the autoregressive Bayesian age-depth
332 modelling algorithm BACON (Blaauw and Christen, 2011). The parameters were adjusted to
333 divide the core into 178 sections of 3 cm depth each and to reflect the relatively stable lake
334 environment, i.e., continuous sedimentation of the organic-rich lacustrine mud (Fig.7).

335 The model output shows that there are two obvious outliers, i.e., extreme age reversals, among
336 the radiocarbon dates (samples CUCA10B-1.5 and CUCA10B-51), which were not used in the
337 age-depth model. From the resulting age-depth model we extracted the age probability
338 distributions for the depth of all clastic layers that were treated as instantaneous deposits (Fig. 7).
339 The uncertainty that arises from the relatively large gap between the core top and the shallowest
340 reliable radiocarbon date (2360 ± 63 years BP) is minimised by the relatively stable sedimentary
341 environment at core site Pos04.

342 The assumption of relatively stable accumulation rates in Pos04 (iv) appears to fail only at the
343 deepest part of the sedimentary record (between clastic layers cN and cO). This becomes evident
344 when comparing the 2 cm thick organic-rich mud interval in core Pos04 with the 43.5 cm thick
345 organic-rich mud interval of the same stratigraphic position in core Pos06. The age-depth model
346 on core Pos04 likely underestimates the time difference between clastic layers cN and cO,
347 because it estimates accumulation rates with constraints on how strongly the accumulation rate
348 may change for each section. Using the average accumulation rate of the entire record down to
349 clastic layer cN at core site Pos06 of $\sim 1.31 \text{ mm yr}^{-1}$ (502 cm of sediment accumulation in 3845
350 years), clastic layer cO is probably ~ 330 years older than clastic layer cN.



351

352 Figure 7: Bayesian age-depth model of core Pos04 in Lake Cucao calculated with BACON
 353 (Blaauw and Christen, 2011). The core surface image and sedimentological core log are
 354 displayed on the left. The tsunami deposits are treated as instantaneous deposits and are
 355 taken out of the core for age-depth modelling. The bottom x-axis shows the model results
 356 for all tsunami deposits as coloured age distributions.

357 5 Discussion

358 5.1 Antidunes as a product of tsunami inundation in Lake Cucao

359 The hummocks with the up-slope dipping internal reflectors below R4 (clastic layer cF) are
360 interpreted as antidunes due to their height and length in combination with the up-slope dipping
361 internal reflectors. Antidunes form in the upper stage supercritical flow regime. The wavelength
362 of antidunes is related to the wavelength of the standing wave that produced them (Allen, 1984),
363 which in turn is proportional to the square of the flow speed during formation (Kennedy, 1963).
364 The resulting relationship between flow speed and wavelength of the antidune bedform is
365 described by Carling (2009) as:

$$366 \quad U = \sqrt{\frac{g L_a}{2\pi}} \quad (1)$$

367 where U is the flow speed, g the gravitational acceleration on earth and L_a the average
368 wavelength in a train of antidune bedforms. The flow depth d in dependence on average
369 wavelength is expressed by

$$370 \quad d = \frac{L_a}{2\pi} \quad (2)$$

371 According to equation (1) the flow speed during antidune formation was $\sim 6.8 \text{ m s}^{-1}$ (24.6 km h^{-1})
372 and according to equation (2) the flow depth was $\sim 4.8 \text{ m}$. Both dimensions compare well with
373 directly measured flow properties of recent large-scale tsunami inundations (cf., Fritz et al.,
374 2006, 2012). The location of the antidunes suggests that the freshwater marsh, which now
375 accommodates the village of Cucao was washed over by strong, certainly destructive water
376 currents. Despite their size, antidunes form relatively quickly once supercritical flow develops.
377 However, with three antidunes of similar shape and size, we argue that supercritical flow was
378 well developed, steady and sustained.

379 5.2 Age control and accumulation rate variability in Lake Cucao

380 There is no overall strong spatial variability in accumulation rate between long cores from the
381 western part of the basin, which is indicated by sub-parallel clastic layers in the core to core
382 correlation. This is confirmed by parallel to sub-parallel reflectors R1 to R5 on reflection-seismic
383 profiles (Fig. 2a, b).

384 There are three exceptions, which are (i) confined areas of erosional truncation in form of small
385 channels (Fig. 2c), (ii) the area close to the crosscutting channel along the northeastern side of
386 the lake, where the sedimentary infill becomes significantly thinner or is non-existent (Fig. 2c,
387 d), and (iii) the deepest part of most long cores, where the strata form onlaps (this includes the
388 age-depth modelled core Pos04 between cN and cO). All long core sites avoid the areas of (i)
389 and (ii).

390 In short cores CUC10 and CUC11, located 2–3 km southeast of most other cores, and where
391 tidal currents are probably weaker or absent, up to 21 cm of organic-rich mud accumulated
392 above the CE 1960 tsunami deposit (Fig. 4). This thickness is comparable to 20–30 cm of post-
393 1960 sediment accumulation in Lake Huelde (Kempf et al., 2015), which is now unaffected by
394 tidal currents. In all other cores farther west in Lake Cucao the same interval is either $\leq 4 \text{ cm}$

395 thick or is missing, showing non-deposition or episodes of erosion in the post-1960 lake
396 environment in the ocean-proximal area of the lake.

397 The age-control of the last 2000 years relies strongly on the assumption of uniform accumulation
398 rates between the CE 1960 tsunami deposit and the uppermost useful radiocarbon date at 246 cm
399 (event-free core depth) (Fig. 7, Table 1). Cores and reflection-seismic profiles justify this
400 interpolation, because of the uniform stratigraphy with little lateral variability in this part of the
401 stratigraphic record of U2 near the coring site Pos04.

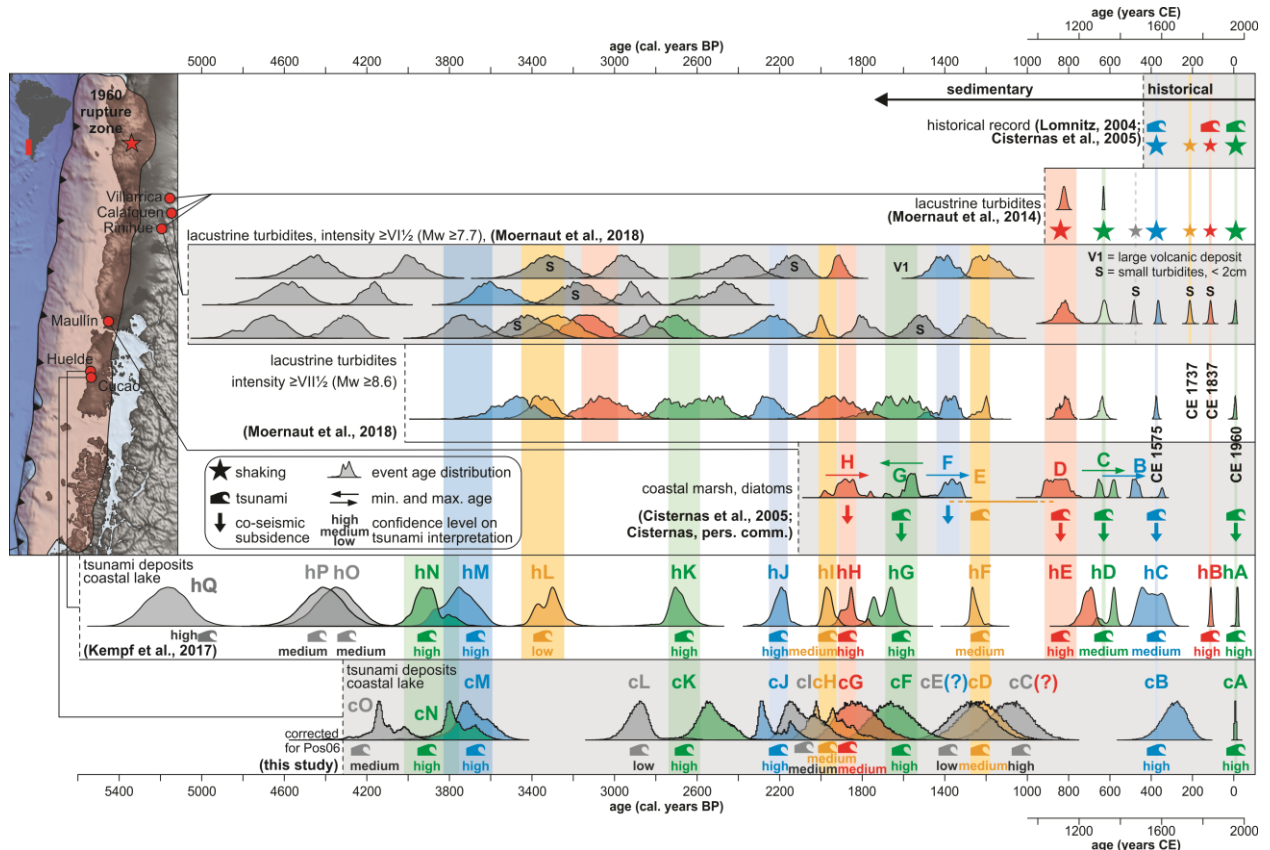
402 Chronologies of other regional paleotsunami and paleoseismic records from south central Chile
403 are based on similar primary age-depth information, i.e., on radiocarbon dates of plants flattened
404 by the tsunami, rootlets in soil, terrestrial plant fragments from the pre- and post-tsunami
405 lacustrine sediment and tephra (Cisternas et al., 2005, 2017; Atwater et al., 2013; Moernaut et
406 al., 2014, 2018; Garrett et al., 2015; Kempf et al., 2017). The uncertainty intervals of tsunami
407 ages in the Lake Cucao record (mean 95% age interval = 318 years) are greater than the
408 uncertainty intervals of the tsunami ages of, for example, the paleotsunami record of Lake
409 Huelde (mean 95% age interval = 203 years) (Kempf et al., 2017). Nevertheless, the Lake Cucao
410 ages correlate well with regional paleotsunami records (Fig. 8). The age-control can be
411 considered of comparable quality.

412 *5.3 Age of the crosscutting channel and constraints on Lake Cucao's vertical displacement* 413 *history*

414 Coastal areas on subduction zones are known to be prone to vertical deformation throughout the
415 seismic cycle (Wesson et al., 2015). The CE 1960 Great Chilean Earthquake caused the area
416 around Lake Cucao to subside co-seismically by ~1 m (Plafker and Savage, 1970), which put
417 Lake Cucao into an intertidal position, if the lake level was not in the intertidal zone before. The
418 subsidence of ~1 m may have intensified the tidal currents, which would explain the limited
419 post-CE 1960 sedimentation in all but the most distal coring sites. Today tidal currents entering
420 the lake during high tide are continuing to form the intertidal delta, the crosscutting channel and
421 the mega-ripples. Given that the sedimentary record below the CE 1960 tsunami deposit appears
422 to have stable accumulation rates, we argue that the vertical position of the river channel in
423 relation to relative sea-level is probably at an extreme low at present with respect to its evolution
424 over the last 4300 years.

425 If the channel would be a recently formed feature, it would truncate the mostly parallel to sub-
426 parallel internal reflectors of seismic unit U2. This is not the case; all internal reflectors, R1 to
427 R5, in U2 converge towards the channel (Fig. 2c), which indicates that intertidal currents were
428 active at least episodically during the period represented by the sedimentary infill visible on
429 reflection-seismic profiles. This constrains the net vertical displacement of Lake Cucao in the
430 last 4300 years to a narrow window around its current position.

431 Additionally, river channels play a primary role in connecting the ocean with coastal lakes
432 during tsunami inundation (Kempf et al., 2015, 2017). Consequently, regardless of the exact
433 position of the coastline and river channel migrations, Lake Cucao may have been a reliable
434 tsunami recorder with relatively stable sensitivity to tsunami inundation in the past 4300 years
435 and potentially longer.



436
 437 *Figure 8: Regional correlation of paleoseismic and paleotsunami records. The instrumental*
 438 *record only includes the CE 1960 event and is not especially listed here. Documented*
 439 *history reveals three more large events in CE1575, 1737, 1837 (Cisternas et al., 2005;*
 440 *Lomnitz, 2004). Lacustrine turbidites from the Chilean lake district give paleoseismic*
 441 *evidence (Moernaut et al., 2018, 2014). The paleotsunami records from Maullín (Cisternas*
 442 *et al., 2005) and Lake Huelde (Kempf et al., 2017) offer the direct comparisons between*
 443 *tsunami deposits. The age of cO is here corrected by 330 yrs because of the regular*
 444 *organic-rich lacustrine sediment between cN and cO in core Pos06 (in contrast to core*
 445 *Pos04 for which the age-depth model was made).*

446 **5.4 Identifying tsunami deposits in the Lake Cucao sedimentary record**

447 The clastic layers share similar sedimentary characteristics to the tsunami deposit of CE 1960.
 448 However, other causative processes must be excluded before a tsunami origin can be assigned.
 449 Tsunami deposits have several sedimentary characteristics, most are site-specific, and few are
 450 unique to tsunami deposits. For example, landwards thinning and landward fining sand sheets
 451 can be produced by storm surges and tsunamis alike (Kortekaas and Dawson, 2007). However,
 452 the relatively distant inland location (~1.3 km between ocean and lake) makes storm deposition
 453 in Lake Cucao unlikely. While storms occur on the south central Chilean coast, the tropical
 454 cyclones with the potential to deposit several kilometres inland and in coastal lakes, have not
 455 been documented and are unlikely to happen, even under strong El Niño conditions (Fedorov et
 456 al., 2010).

457 Excluding competing hypotheses for the formation of similar layers is equally valuable. For
 458 Lake Cucao we can, for example, exclude flood turbidites, which are not uncommon in Chilean

459 lakes (e.g., Van Daele et al., 2019), because upstream adjacent Lake Huillinco traps riverine
460 flood input to Lake Cucao, which reduces the direct riverine input to Lake Cucao to a small
461 creek that enters Lake Cucao from the south in its eastern part. The small creek does not have a
462 large enough catchment to produce lake-wide flood turbidites. And if it were to produce flood
463 turbidites the fining of sediment would be away from the inflow of the creek, i.e., east to west in
464 the study area and not west to east.

465 We define the following five criteria for the sedimentary environment of Lake Cucao, which are
466 either indicative of tsunami deposition or can be used to exclude other processes.

- 467 i) *High magnetic susceptibility* – Magnetic susceptibility is controlled by the ferrimagnetic
468 mineral content of the sediment. High magnetic susceptibility in Lake Cucao means the
469 sediment contains iron oxides (i.e., hematite and magnetite). The concentrations of
470 ferrimagnetic minerals in the basin of Lake Cucao can be increased by organic matter
471 depletion, compaction or by deposition of iron oxides. The low magnetic susceptibility
472 values of organic-rich mud and the sometimes extremely high values of magnetic
473 susceptibility in the clastic layers suggest that the layers with high magnetic susceptibility
474 values are from extra-lacustrine sources. Processes that could provide such a sediment
475 source are limited to lake-inundating events, such as storms and tsunamis. This effect has
476 been described for the CE 1960 tsunami deposit (Kempf et al., 2015).
- 477 ii) *Lateral traceability in the sedimentary record* – Tsunami deposits in coastal lakes are
478 spatially variable in thickness (Kelsey et al., 2005; Kempf et al., 2017). However,
479 tsunami deposits are often continuous deposits to where they wedge out towards their
480 maximum lateral extent. When tsunamis inundate coastal lakes, the water flow contains
481 sand and deposits it, remobilises muddy lake sediment and redistributes it within the lake
482 basin. Areas beyond the zone of sandy deposition can receive exclusively muddy tsunami
483 sediment (Kelsey et al., 2005; Kempf et al., 2015, 2017). Therefore, tsunami deposits
484 should be laterally traceable in the sedimentary record throughout large areas of the lake,
485 if not the entire lake basin. The criterion is expressed as a fraction of the number of cores
486 that contain the clastic layer over the number of cores that contain the stratigraphic
487 interval of the clastic layer. Complete or nearly complete representation in the
488 sedimentary archive is treated as indicative for tsunami deposition (Fig. 4).
- 489 iii) *Acoustic reflector correlation* – The six strong reflectors (R1–R6) on the reflection-
490 seismic profiles represent strong contrasts in acoustic impedance, i.e., differences in p-
491 wave velocity and/or density. In an organic-rich mud-dominated environment high
492 acoustic impedance contrast can be associated with clastic layers. Not every clastic layer
493 will necessarily produce a high-amplitude reflector, but if a clastic layer can be correlated
494 to a basin-wide high-amplitude acoustic reflector, then this points towards basin wide
495 distribution and high clastic content, which is expected from a tsunami deposit.
- 496 iv) *Mud rip-up clasts* – We interpret the mud clasts as mud rip-up clasts. Mud rip-up clasts
497 are generated by high-energy processes in otherwise low-energy environments. In
498 subaqueous landslides, mud rip-up clasts occur on the spectrum of disintegration of the
499 sliding sediment from slumps, to debris flows, to turbidity currents (cf., Lee et al., 2013).
500 Onshore landslides that impact muddy fjord sediment have also produced mud rip-up

501 clasts, which may show paleo flow direction by imbrication (Van Daele et al., 2014). In
502 fluvial systems mud rip-up clasts are associated with cut bank collapses of muddy soils.
503 In coastal environments, like marshes, mud rip-up clasts are commonly associated with
504 tsunami deposition (Peters et al., 2007), however, storm surges reportedly can also
505 produce mud rip-up clasts (Phantuwongraj et al., 2013). In Lake Cucao, two types of mud
506 rip-up clasts can be differentiated by their radiodensity. One type has the same
507 radiodensity as the lacustrine organic-rich mud and is interpreted as originating from bulk
508 erosion of the lake basin sediment. The other type has higher radiodensity and could
509 represent soil from the lake-surrounding marshes. Similar variations in mud rip-up clasts
510 were described in trenches on the Chilean main land near Maullín (Atwater et al., 2013).
511 Specifically for Lake Cucao, the presence of both types of mud rip-up clasts (Fig. 5c)
512 excludes strong tidal currents and slope failure turbidites. Tidal currents could work
513 similar to fluvial systems with regard to the erosion of source material of mud rip-up
514 clasts and to deposition of clastic layers.

515 v) *Age-correlation* – Megathrust earthquake-induced tsunamis affect long stretches of
516 coastline. Tsunami deposits can therefore be correlated over long distances using their
517 chronology (Peters et al., 2007; Cisternas et al., 2017). If a clastic layer correlates in age
518 to an identified tsunami deposit elsewhere in south central Chile, then this supports the
519 interpretation as a tsunami deposit. In the Lake Cucao sedimentary record, the
520 interpretation of the CE 1960 tsunami deposit was partially based on such an age
521 correlation (Kempf et al., 2015). Downcore, age-correlation with the Lake Huelde
522 sedimentary record (Kempf et al., 2017) is especially interesting, because of the lakes’
523 proximity (2 km) to each other and the similarity of the paleotsunami record, despite the
524 difference in lacustrine sedimentary environments.

525 Two of the 15 clastic layers (cE and cL) fulfil only one or no criteria at all. The confidence of an
526 interpretation as a tsunami deposit in these cases is low, however, a tsunami origin is probably
527 still the most favourable hypothesis (Table 2). Eight clastic layers fulfil three or more criteria and
528 the confidence level for interpreting these layers as tsunami deposits is high. The remaining five
529 clastic layers fulfil two criteria sufficiently and receive a medium confidence level.

530 The Lake Cucao record potentially matches with 10 regionally known paleotsunami and
531 paleoseismic events (Fig. 8, Table 3). Additionally, deposit cC matches to some extent with
532 deposit hE in Lake Huelde and event D in Maullín (Fig. 8), but weaker age control in the Lake
533 Cucao record for the last ~2000 years may inhibit a conclusive correlation. The confidence level
534 for both event deposits hE and cC are high, which supports the hypothesis of a similar origin,
535 because in no other instance is there a high confidence tsunami deposit in Lake Huelde without a
536 matching tsunami deposit in Lake Cucao, and vice versa. The only exception is the cryptic CE
537 1837 tsunami deposit, that was recognised in Lake Huelde by IRSL dating (Kempf et al., 2017).

538 Deposit cE matches well with event F in Maullín, however, Lake Huelde does not record
539 tsunami deposition in this period and in Maullín the event was only recognised by co-seismic
540 subsidence and not with a tsunami deposit (Cisternas et al., 2005; Kempf et al., 2017) (Table 3).
541 Either Lake Cucao was relatively sensitive to tsunami inundation, e.g., relatively high sea-level,
542 at the time and recorded a minor tsunami that had no sedimentary impact in Maullín, Lake

543 Huelde and other regional paleotsunami records. Or as the low confidence level denotes, deposit
544 cE is potentially not a tsunami deposit.

545 Both deposits cL and hL have only a minor sedimentary imprint in Lake Cucao and Lake
546 Huelde, respectively, with low confidence level on the interpretation as tsunami deposits (cf.,
547 Kempf et al., 2017). If either deposit is a tsunami deposit, then the origin is probably a minor
548 tsunami. The age-depth modelling in both records does not match the two deposits, so that it can
549 be concluded that they are most likely not from the same event.

550 In contrast, deposits cK and hK from Lake Cucao and Lake Huelde, respectively, share a similar
551 clear (high confidence level), but not extreme sedimentary imprint in their respective records.
552 The age-depth models match the two deposits, so it is likely that cK and hK were deposited
553 during the same tsunami inundation event.

554 *Table 3: Regional age-correlation of paleotsunami and paleoseismic events. Bold events are*
555 *correlated across the three regional paleotsunami records from Maullín, Lake Huelde and*
556 *Lake Cucao.*

historical record	Cucao	Huelde	Maullín	Rinihue
				Calafquen
				Villarrica
year of event CE	name in record (confidence level)	name in record (confidence level)	name in record	correlating event
1960	cA (high)	hA (high)	A	yes
1837	-	hB (high)	-	yes
1737	-	-	-	yes
1575	cB (high)	hC (medium)	B	yes
beyond record	-	hD (medium)	C	yes
	cC (high) (?)	hE (high)	D	yes
	cD (medium)	hF (medium)	E	yes
	cE (low) (?)	-	F	(?)
	cF (high)	hG (high)	G	yes
	cG (medium)	hH (high)	H	yes
	cH (medium)	hI (medium)	beyond record	yes
	cl (medium)	-		(?)
	cJ (high)	hJ (high)		yes
	cK (high)	hK (high)		yes
	cL (low)	-		no
	-	hL (low)		yes
	cM (high)	hM (high)		yes
	cN (high)	hN (high)		(?)
	cO (medium)	-		(?)
	beyond record	hO (medium)		(?)
		hP (medium)		(?)
		hQ (high)		beyond record

557

558 *5.5 Spatial perspective on tsunami deposits in a lake basin*

559 Event maps (Figs. 9, 10) summarise the sedimentary characteristics of the tsunami deposits and
560 visualise spatial trends of the tsunami deposits. The following conclusions are supported by the
561 spatial data:

- 562 i) Mud rip-up clasts are limited to the proximal part of the lake basin (Fig. 9). The
563 tsunami deposit cO at core site Pos04 is the only exception. This seems plausible as it
564 requires high energy water flow to erode and transport mud rip-up clasts. Dissipating
565 energy in fluid flow over distance would dictate that mud rip-up clasts would be the
566 first particles to resist transport or remobilisation.
- 567 ii) For a large extent in the lake basin, tsunami deposits do not decrease in thickness.
568 This contradicts the spatial trend in onshore tsunami deposits, where tsunami deposit
569 thickness is influenced by the onshore morphology and tends to decrease with
570 increasing run-up distance (Goto et al., 2014). This study has thickness data along up
571 to ~3 km of inundation distance. Even for the tsunami deposit thickness data from CE
572 1960 and CE 1575 (cB) with a ~3 km long transect, no decreasing trend in thickness
573 can be recognised. Logically, in the most distal parts of the record the tsunami deposit
574 must wedge out, however, the core sites are not located in the area where this occurs.
575 The trend of landward thinning observed in onshore environments is ascribed to a
576 loss of flow energy over inundation distance. There is increasing incorporation of
577 lacustrine mud in the tsunami flow over inundation distance in Lake Cucao. The finer
578 grain sizes can be transported with much lower flow energy. This may be the effect
579 that mitigates landward thinning in lacustrine environments.
- 580 iii) From the location where a tsunami deposit has a muddy component, the muddy
581 characteristic of the tsunami deposits is always present in more distal locations.
582 Examples are the tsunami deposits cF, cK or cM.
- 583 iv) Less energetic tsunamis can produce muddy tsunami deposits over large parts of a
584 lacustrine basin, e.g., tsunami deposit cD (Fig. 9). However, detection of those
585 exclusively muddy tsunami deposits is more difficult, because of the similarities to
586 lacustrine sediments. In the case of the muddy tsunami deposits in Lake Cucao, the
587 magnetic susceptibility was used to locate candidate clastic layers. In environments
588 where magnetic susceptibility cannot be used, other methods need to be tested, e.g.,
589 XRF scanning or bio-marker analysis.

590 *5.6 A conceptual model towards the origin and evolution of the lake basin*

591 In order to develop a conceptual stratigraphic model of Lake Cucao that incorporates all
592 sedimentologic evidence available, we begin with the topographical depression that is now
593 occupied by Lake Cucao. The depression was a glacifluvial river valley (Glasser et al., 2008),
594 which was submerged during the last global postglacial eustatic sea-level rise (Siddall et al.,
595 2003). During this transgression, the glacifluvial valley must have become an estuary, a similar
596 evolution to lakes Lanahue and Lleu Lleu ~500 km farther north (Stefer et al., 2010) (Fig. 1).
597 The oldest recovered sediment in core Pos04 (around tsunami deposit cN, reflector R6) is
598 lacustrine, indicating that the barrier, which makes Lake Cucao a coastal lake rather than an
599 estuary, has been in place earlier than 4300 years ago.

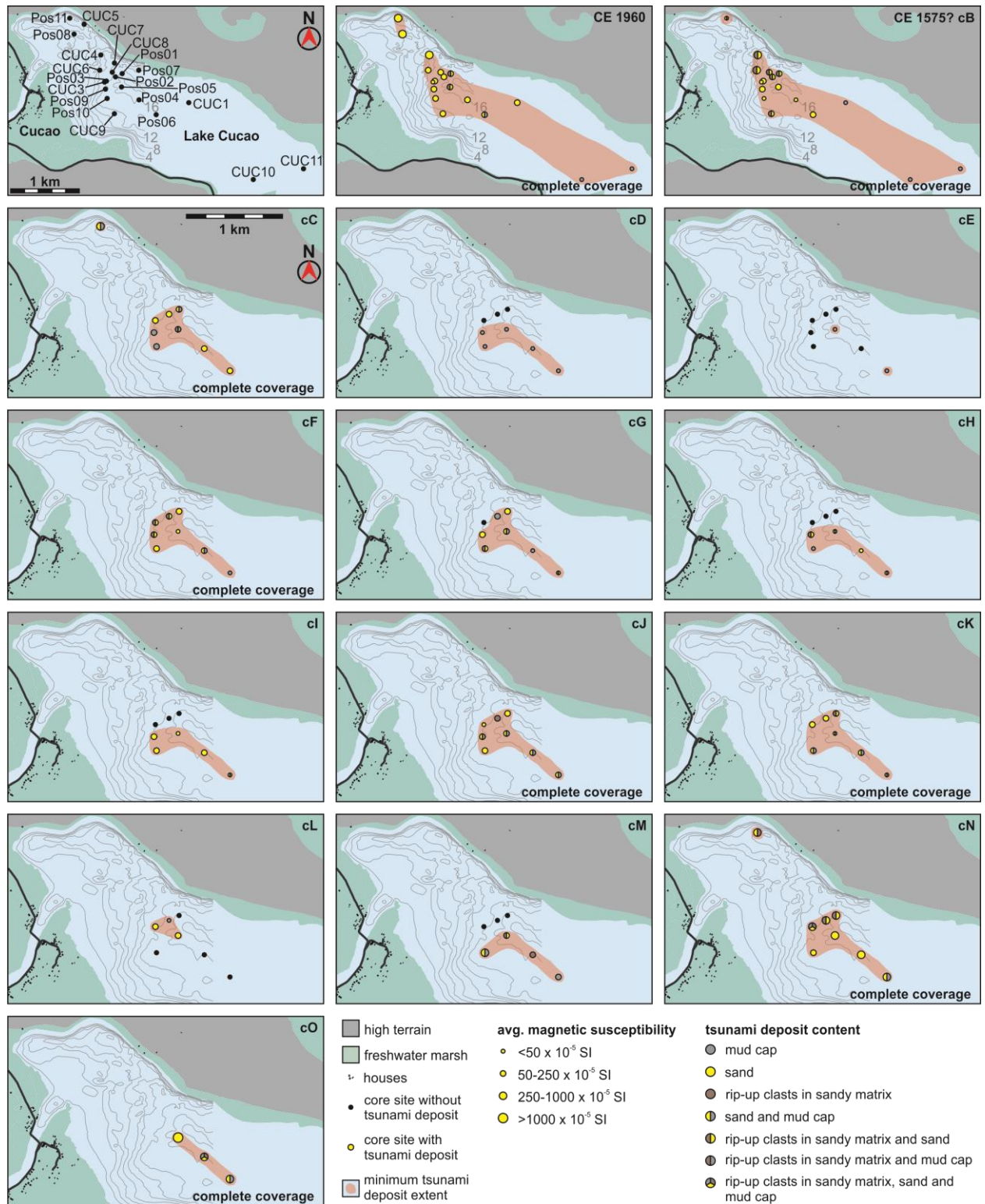
600 Most likely aeolian sedimentation created the barrier and therewith enclosed the estuary to
601 become a lake basin. The timing of the sill formation is unclear, however, one plausible
602 hypothesis is that the expanding westerlies between 8.5 and 5.5 ka (Lamy et al., 2010) may have
603 enabled aeolian processes to create the sill. Aeolian processes are still prevailing in the coastal
604 area west of Lake Cucao evidenced by an active dune belt.

605 Currently, Lake Cucao lies in the intertidal zone (Villalobos et al., 2003; Kempf et al., 2015),
606 with saline water flowing into the lake from the Pacific during high tides. This process has been
607 active at least sporadically since 4300 cal. years BP, evidenced by the convergent internal
608 reflectors in the entire sediment sequence of U2 near the tidal channel. The same process has
609 built up a tidal delta in Lake Cucao around the outlet. The conceptual stratigraphic model
610 includes foresets of the tidal delta interfingering with lake basin and estuarine sediments (Fig.
611 11). One of these foresets may explain the muddy sand with the same characteristics as the
612 exposed tidal delta sediments at the base of cores Pos02, Pos03 and Pos11 (Fig. 4). Clastic layer
613 cN, interpreted as a tsunami deposit, is in direct contact with the muddy sand in all cores of the
614 western part of the basin, except at Pos06. It appears that the formation of cN disrupted the
615 deposition of muddy sand at the mentioned core locations. Clastic layer cN is thicker and coarser
616 than all other clastic layers in most core locations. Additionally, the deposit correlates
617 chronologically to deposit hN, which is among the thicker and coarser tsunami deposits from the
618 nearby Lake Huelde paleotsunami record (Kempf et al., 2017).

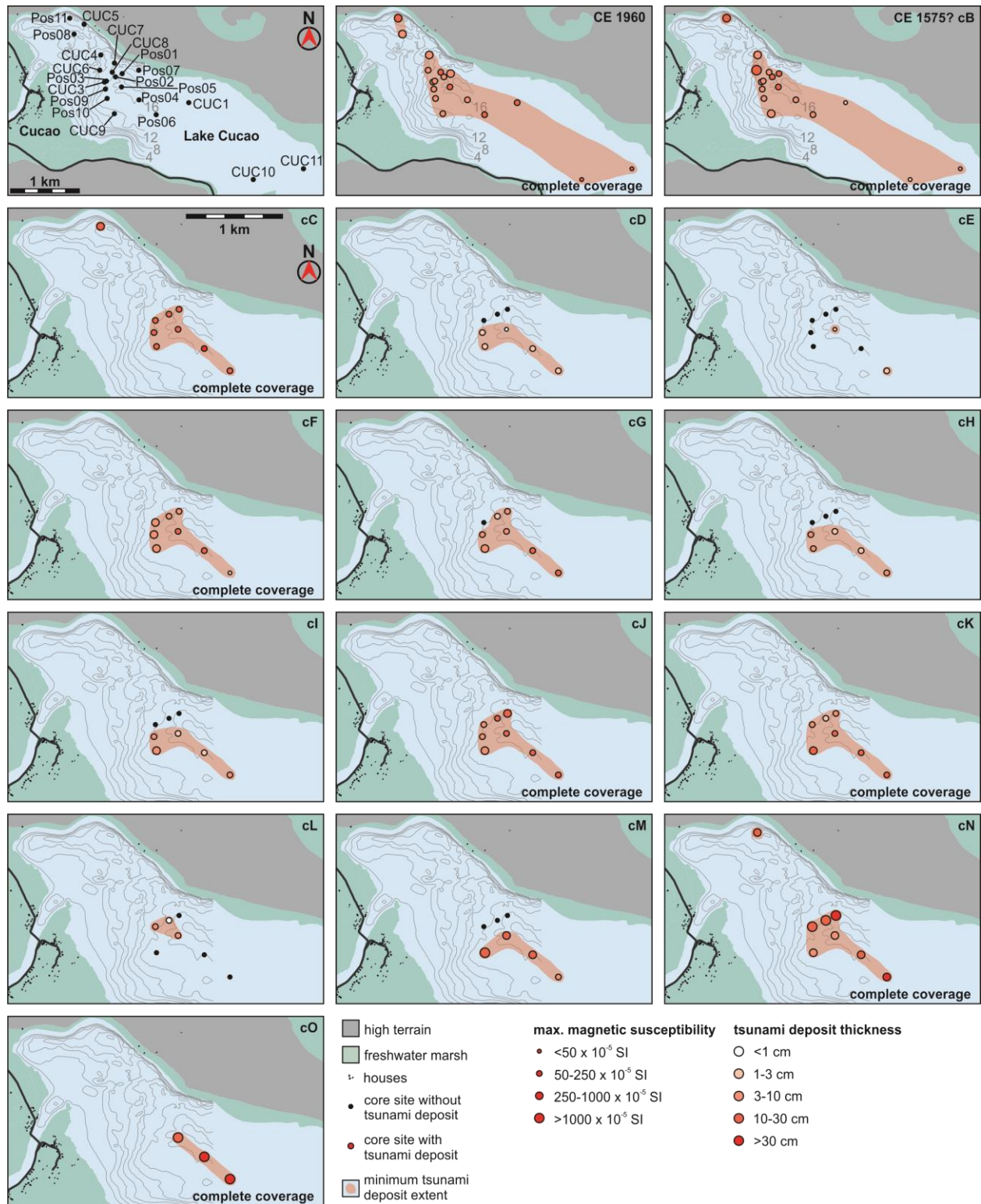
619 The overall extreme character relative to other tsunami deposits in the respective records of cN
620 and hN may point towards an unusually large tsunami. The end of foreset sedimentation after
621 deposition of cN could be due to a large amount of either co-seismic uplift or subsidence during
622 this event.

623 In the uplift scenario the lake system may stop interacting with the Pacific Ocean altogether.
624 Tidal inflows into the lake would not occur and the processes, which form topsets and foresets
625 on the tidal delta, would stop. Large amounts of co-seismic uplift can occur on the Chilean coast,
626 e.g., 3 to 4 m in CE 1960 on Isla Guafo (Sievers et al., 1963). However, the geometry of the
627 crust on and off Chiloé Island probably needs splay fault slip to generate such an uplift and none
628 of the earthquakes in CE 1960, 1837 or 1575 created large (> 1 m) co-seismic uplift on the west
629 coast of Chiloé Island (Sievers et al., 1963; Plafker and Savage, 1970; Garrett et al., 2015;
630 Cisternas et al., 2017).

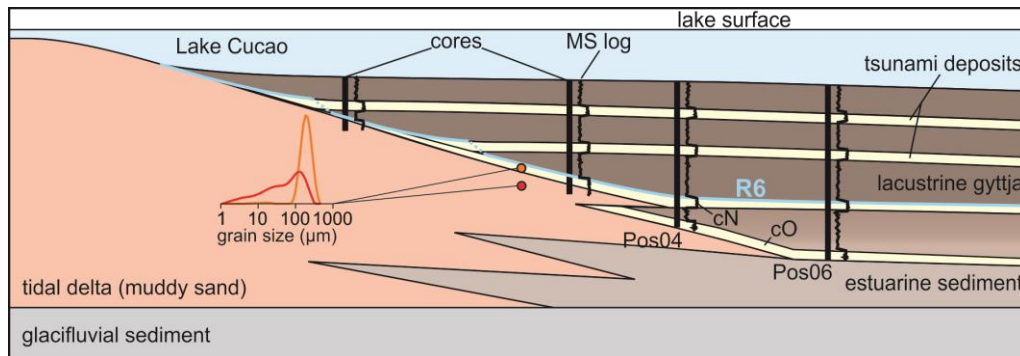
631 The subsidence scenario seems more plausible, because of the example given by co-seismic
632 subsidence around Cucao (~1 m) during the CE 1960 earthquake (Plafker and Savage, 1970).
633 The subsidence would create accommodation, which would favour aggradation at the cost of
634 progradation of the delta. During aggradation on the delta, the lake basin would accumulate
635 organic-rich mud. Once aggradation used up the newly available accommodation, the delta
636 would switch back to progradation and begin forming the next interfingering foreset. In both
637 examples, the presence of the tidal delta would be less dominant in the basinal sediments.



638
 639 *Figure 9: Event map of all tsunami deposit cA, i.e. CE 1960, to cO. The dots refer to core sites*
 640 *that contain the stratigraphic interval in which the tsunami deposit is located. Black dots*
 641 *mean the tsunami deposit was not detected. The size of the dot is a function of the average*
 642 *magnetic susceptibility over the entire tsunami deposit. The colour of the dot is a function of*
 643 *the sedimentary content of the tsunami deposit. The red polygon depicts the lateral extent of*
 644 *the tsunami deposit.*



645
 646 *Figure 10: Event map of all tsunami deposit cA, i.e. CE 1960, to cO. The dots refer to core sites*
 647 *that contain the stratigraphic interval in which the tsunami deposit is located. Black dots*
 648 *mean the tsunami deposit was not detected. The size of the dot is a function of the maximum*
 649 *magnetic susceptibility of the tsunami deposit. The colour of the dot is a function of the*
 650 *tsunami deposit thickness in the core (darker red means thicker tsunami deposit). The red*
 651 *polygon depicts the lateral extent of the tsunami deposit.*



652

653 *Figure 11: Conceptual stratigraphic model of Lake Cucao's sedimentary infill that summarizes*
654 *the sedimentologic evidence available in the literature and in the results of this study. This*
655 *model also explains the corrected age of tsunami deposit cO.*

656 6 Conclusions

657 Based on reflection-seismic profiles and numerous sediment cores, we add a new, long and
658 continuous paleotsunami record in the rupture zone of the CE 1960 Great Chile Earthquake. We
659 present the following conclusions:

- 660 i) Reflection-seismic profiles are crucial to understand the dynamic sedimentary system of
661 coastal lakes and to help in selecting the most appropriate coring locations for
662 paleotsunami research. Moreover, reflection-seismic profiles may reveal sedimentary
663 structures which can allow quantification of flow speed and depth, e.g., antidunes (Fig.
664 2).
- 665 ii) Dynamic coastal lakes with daily tidal inflow can be used for extracting long
666 paleotsunami records. For the last 4300 years, Lake Cucao presents 15 tsunami deposits
667 of mostly moderate to high confidence in interpretation. This confidence level was based
668 on physical sedimentary characteristics and contextual characteristics (Table 2), such as
669 maximum magnetic susceptibility, traceability (Figs. 9, 10), correlation to acoustic
670 reflectors on the reflection-seismic profiles (Fig. 6), the presence or lack of mud rip-up
671 clasts (Figs. 5, 9), and age correlation with regional paleotsunami (Fig. 8). At least 10
672 interpreted tsunami deposits correlate to paleotsunami deposits found in nearby Lake
673 Huelde.
- 674 iii) The most complete tsunami record was found in core Pos05, 1.3 km from the lake outlet
675 (tidal inlet) and a total 2.6 km from the present-day coastline. This relatively far inland
676 location for regular tsunami deposition is facilitated by the river channel. There is
677 evidence for tidal currents throughout the entire record, and thus persistent river
678 connection, which allowed for continuous recording of tsunamis, despite co-, post- and
679 inter-seismic relative sea-level change in the late Holocene. However, such tidal currents
680 can affect sediment dynamics, leading to variable depositional rates in space and time,
681 adding complexity for reliable mapping and dating of tsunami deposits.
- 682 iv) This study underlines the many challenges and extraordinary advantages associated to
683 paleotsunami research on coastal lakes and demonstrates how indispensable geophysical
684 mapping and numerous coring sites are in understanding the depositional environment of
685 dynamic coastal lakes for extracting high-quality, long and continuous paleotsunami
686 records.

687 **Acknowledgments**

688 PK acknowledges financial support by the Special Research Fund of Ghent University (BOF),
689 JM from the Chilean Fondecyt projects nr. 1150346 and 1150321, MVD from the Research
690 Foundation Flanders (FWO travel grant K201512N), RU from CONICYT/FONDAP/15130015.
691 We thank Koen De Rycker, Willem Vandoorne and Gauvain Wiemer for fieldwork support, Dr.
692 Claire Schepens and Dr. Eric Achten for CT-scanner support. IHS Markit is acknowledged for
693 providing the Kingdom seismic interpretation software within their educational grant program.
694 We thank Dr. Pedro Costa, Dr. Witold Szczuciński and Dr. Jasper Knight for constructive
695 reviews to the manuscript.

696 **References**

- 697 Allen, J.R.L., 1984. *Sedimentary Structures: Their Character and Physical Basis*. Elsevier,
698 Amsterdam.
- 699 Amante, C., Eakins, B.W., 2009. ETOPO1 1 Arc-Minute Global Relief Model: Procedures, Data
700 Sources and Analysis. NOAA Technical Memorandum NESDIS NGDC-24. National
701 Geophysical Data Center, NOAA, doi:10.7289/V5C8276M.
- 702 Atwater, B.F., Cisternas, M., Yulianto, E., Prendergast, A.L., Jankaew, K., Eipert, A.A.,
703 Ignatius, W., Fernando, S., Tejakusuma, I., 2013. The 1960 tsunami on beach-ridge plains
704 near Maullín, Chile: Landward descent, renewed breaches, aggraded fans, multiple
705 predecessors. *Andean Geology* 40, 393–418.
- 706 Blaauw, M., Christen, J.A., 2011. Flexible Paleoclimate Age-Depth Models Using an
707 Autoregressive Gamma Process. *Bayesian Analysis* 6, 457–474.
- 708 Carling, P., Burr, D., Brennand, T.A., 2009. A review of open-channel megaflood depositional
709 landforms on Earth and Mars. In: Burr, D.M., Carling, P.A., Baker, V.R. (Eds.),
710 *Megaflooding on Earth and Mars*. Cambridge University Press, Cambridge, pp. 33–49.
- 711 Chagué-Goff, C., Schneider, J.-L., Goff, J.R., Dominey-Howes, D., Strotz, L., 2011. Expanding
712 the proxy toolkit to help identify past events — Lessons from the 2004 Indian Ocean
713 Tsunami and the 2009 South Pacific Tsunami. *Earth-Science Reviews* 107, 107–122.
- 714 Chagué-Goff, C., Szczuciński, W., Shinozaki, T., 2017. Applications of geochemistry in tsunami
715 research: A review. *Earth-Science Reviews* 165, 203–244.
- 716 Cisternas, M., Atwater, B.F., Torrejón, F., Sawai, Y., Machuca, G., Lagos, M., Eipert, A.,
717 Youlton, C., Salgado, I., Kamataki, T., Shishikura, M., Rajendran, C.P., Malik, J.K., Rizal,
718 Y., Husni, M., 2005. Predecessors of the giant 1960 Chile earthquake. *Nature* 437, 404–
719 407.
- 720 Cisternas, M., Garrett, E., Wesson, R., Dura, T., Ely, L.L., 2017. Unusual geologic evidence of
721 coeval seismic shaking and tsunamis shows variability in earthquake size and recurrence in
722 the area of the giant 1960 Chile earthquake. *Marine Geology* 385, 101–113.
- 723 Costa, P.J.M., Costas, S., González-Villanueva, R., Oliveira, M.A., Roelvink, D., Andrade, C.,
724 Freitas, M.C., Cunha, P.P., Martins, A., Buylaert, J.-P., Murray, A., 2016. How did the AD
725 1755 tsunami impact on sand barriers across the southern coast of Portugal?

- 726 Geomorphology 268, 296–311.
- 727 Dura, T., Cisternas, M., Horton, B.P., Ely, L.L., Nelson, A.R., Wesson, R.L., Pilarczyk, J.E.,
728 2015. Coastal evidence for Holocene subduction-zone earthquakes and tsunamis in central
729 Chile. *Quaternary Science Reviews* 113, 93–111.
- 730 Dura, T., Engelhart, S.E., Vacchi, M., Horton, B.P., Kopp, R.E., Peltier, W.R., Bradley, S., 2016.
731 The Role of Holocene Relative Sea-Level Change in Preserving Records of Subduction
732 Zone Earthquakes. *Current Climate Change Reports* 2, 86–100.
- 733 Ely, L.L., Cisternas, M., Wesson, R.L., Dura, T., 2014. Five centuries of tsunamis and land-level
734 changes in the overlapping rupture area of the 1960 and 2010 Chilean earthquakes. *Geology*
735 42, 995–998.
- 736 Fedorov, A.V, Brierley, C.M., Emanuel, K., 2010. Tropical cyclones and permanent El Niño in
737 the early Pliocene epoch. *Nature* 463, 1066–1070.
- 738 Fritz, H.M., Borrero, J.C., Synolakis, C.E., Yoo, J., 2006. 2004 Indian Ocean tsunami flow
739 velocity measurements from survivor videos. *Geophysical Research Letters* 33, L24605,
740 doi: 10.1029/2006GL026784.
- 741 Fritz, H.M., Phillips, D.A., Okayasu, A., Shimosono, T., Liu, H., Mohammed, F., Skanavis, V.,
742 Synolakis, C.E., Takahashi, T., 2012. The 2011 Japan tsunami current velocity
743 measurements from survivor videos at Kesennuma Bay using LiDAR. *Geophysical*
744 *Research Letters* 39, L00G23, doi:10.1029/2011GL050686.
- 745 Garrett, E., Shennan, I., Woodroffe, S.A.A., Cisternas, M., Hocking, E.P.P., Gulliver, P., 2015.
746 Reconstructing paleoseismic deformation, 2: 1000 years of great earthquakes at Chucalén,
747 south central Chile. *Quaternary Science Reviews* 113, 112–122.
- 748 Glasser, N.F., Jansson, K.N., Harrison, S., Kleman, J., 2008. The glacial geomorphology and
749 Pleistocene history of South America between 38°S and 56°S. *Quaternary Science Reviews*
750 27, 365–390.
- 751 Goto, K., Hashimoto, K., Sugawara, D., Yanagisawa, H., Abe, T., 2014. Spatial thickness
752 variability of the 2011 Tohoku-oki tsunami deposits along the coastline of Sendai Bay.
753 *Marine Geology* 358, 38–48.
- 754 Heiri, O., Lotter, A.F., Lemcke, G., 2001. Loss on ignition as a method for estimating organic
755 and carbonate content in sediments : reproducibility and comparability of results. *Journal of*
756 *Paleolimnology* 25, 101–110.
- 757 Hogg, A.G., Hua, Q., Blackwell, P.G., Niu, M., Buck, C.E., Guilderson, T.P., Heaton, T.J.,
758 Palmer, J.G., Reimer, P.J., Reimer, R.W., Turney, C.S.M., Zimmerman, S.R.H., 2013.
759 SHCal13 Southern Hemisphere Calibration, 0–50,000 Years cal BP. *Radiocarbon* 55, 1889–
760 1903.
- 761 Kelsey, H.M., Engelhart, S.E., Pilarczyk, J.E., Horton, B.P., Rubin, C.M., Daryono, M.R.,
762 Ismail, N., Hawkes, A.D., Bernhardt, C.E., Cahill, N., 2015. Accommodation space,
763 relative sea level, and the archiving of paleo-earthquakes along subduction zones. *Geology*

- 764 43, 675–678.
- 765 Kelsey, H.M., Nelson, A.R., Hemphill-Haley, E., Witter, R.C., 2005. Tsunami history of an
766 Oregon coastal lake reveals a 4600 yr record of great earthquakes on the Cascadia
767 subduction zone. *Geological Society of America Bulletin* 117, 1009–1032.
- 768 Kempf, P., 2016. Tsunamis in south central Chile: evidence from coastal lakes. Doctoral Thesis,
769 Ghent University, Ghent, Belgium.
- 770 Kempf, P., Moernaut, J., Van Daele, M., Vermassen, F., Vandoorne, W., Pino, M., Urrutia, R.,
771 Schmidt, S., Garrett, E., De Batist, M., 2015. The sedimentary record of the 1960 tsunami
772 in two coastal lakes on Isla de Chiloé, south central Chile. *Sedimentary Geology* 328, 73–
773 86.
- 774 Kempf, P., Moernaut, J., Van Daele, M., Vandoorne, W., Pino, M., Urrutia, R., De Batist, M.,
775 2017. Coastal lake sediments reveal 5500 years of tsunami history in south central Chile.
776 *Quaternary Science Reviews* 161, 99–116.
- 777 Kempf, P., Moernaut, J., Batist, M. De, 2018. Bimodal Recurrence Pattern of Tsunamis in
778 South-Central Chile: A Statistical Exploration of Paleotsunami Data. *Seismological*
779 *Research Letters* 90, 194–202.
- 780 Kennedy, J., 1963. The mechanics of dunes and antidunes in erodible-bed channels. *Journal of*
781 *Fluid Mechanics* 16, 521–544.
- 782 Kortekaas, S., Dawson, A.G., 2007. Distinguishing tsunami and storm deposits: An example
783 from Martinhal, SW Portugal. *Sedimentary Geology* 200, 208–221.
- 784 Lamy, F., Kilian, R., Arz, H.W., Francois, J.-P., Kaiser, J., Prange, M., Steinke, T., 2010.
785 Holocene changes in the position and intensity of the southern westerly wind belt. *Nature*
786 *Geoscience* 3, 695–699.
- 787 Lee, Sang Hoon, Jung, W.-Y., Bahk, J.J., Gardner, J.M., Kim, J.K., Lee, Su Hwan, 2013.
788 Depositional features of co-genetic turbidite–debrite beds and possible mechanisms for their
789 formation in distal lobated bodies beyond the base-of-slope, Ulleung Basin, East Sea (Japan
790 Sea). *Marine Geology* 346, 124–140.
- 791 Lomnitz, C., 1970. Major Earthquakes and Tsunamis in Chile during the period 1535 to 1955.
792 *Geologische Rundschau* 59, 938–960.
- 793 Lomnitz, C., 2004. Major Earthquakes of Chile: A Historical Survey, 1535-1960. *Seismological*
794 *Research Letters* 75, 368–378.
- 795 Moernaut, J., Van Daele, M., Heirman, K., Fontijn, K., Strasser, M., Pino, M., Urrutia, R., De
796 Batist, M., 2014. Lacustrine turbidites as a tool for quantitative earthquake reconstruction:
797 New evidence for a variable rupture mode in south central Chile. *Journal of Geophysical*
798 *Research: Solid Earth* 119, 1607–1633.
- 799 Moernaut, J., Van Daele, M., Fontijn, K., Heirman, K., Kempf, P., Pino, M., Valdebenito, G.,
800 Urrutia, R., Strasser, M., De Batist, M., 2018. Larger earthquakes recur more periodically:
801 New insights in the megathrust earthquake cycle from lacustrine turbidite records in south-

- 802 central Chile. *Earth and Planetary Science Letters* 481, 9–19.
- 803 Moreno, M.S., Bolte, J., Klotz, J., Melnick, D., 2009. Impact of megathrust geometry on
804 inversion of coseismic slip from geodetic data: Application to the 1960 Chile earthquake.
805 *Geophysical Research Letters* 36, L16310, doi:10.1029/2009GL039276.
- 806 Nentwig, V., Bahlburg, H., Górecka, E., Huber, B., Bellanova, P., Witkowski, A., Encinas, A.,
807 2018. Multiproxy analysis of tsunami deposits—The Tirúa example, central Chile.
808 *Geosphere* 14, 1067–1086.
- 809 Nentwig, V., Tsukamoto, S., Frechen, M., Bahlburg, H., 2015. Reconstructing the tsunami
810 record in Tirúa, Central Chile beyond the historical record with quartz-based SAR-OSL.
811 *Quaternary Geochronology* 30, 299–305.
- 812 Peters, R., Jaffe, B., Gelfenbaum, G., 2007. Distribution and sedimentary characteristics of
813 tsunami deposits along the Cascadia margin of western North America. *Sedimentary*
814 *Geology* 200, 372–386.
- 815 Phantuwongraj, S., Choowong, M., Nanayama, F., Hisada, K.-I., Charusiri, P., Chutakositkanon,
816 V., Pailoplee, S., Chabangbon, A., 2013. Coastal geomorphic conditions and styles of storm
817 surge washover deposits from Southern Thailand. *Geomorphology* 192, 43–58.
- 818 Plafker, G., Savage, J.C., 1970. Mechanism of the Chilean Earthquakes of May 21 and 22, 1960.
819 *Geological Society of America Bulletin* 81, 1001–1030.
- 820 Reinhardt, E.G., Nairn, R.B., Lopez, G., 2010. Recovery estimates for the Río Cruces after the
821 May 1960 Chilean earthquake. *Marine Geology* 269, 18–33.
- 822 Siddall, M., Rohling, E.J., Almogi-Labin, A., Hemleben, C., Meischner, D., Schmelzer, I.,
823 Smeed, D.A., 2003. Sea-level fluctuations during the last glacial cycle. *Nature* 423, 853–
824 858.
- 825 Sievers, H., Villegas, G.C., Barros, G., 1963. The seismic sea wave of 22 May 1960 along the
826 Chilean coast. *Bulletin of the Seismological Society of America* 53, 1125–1190.
- 827 Stefer, S., Moernaut, J., Melnick, D., Echtler, H.P., Arz, H.W., Lamy, F., De Batist, M., Oncken,
828 O., Haug, G.H., 2010. Forearc uplift rates deduced from sediment cores of two coastal lakes
829 in south-central Chile. *Tectonophysics* 495, 129–143.
- 830 Szczuciński, 2020. Postdepositional changes to tsunami deposits and their preservation potential.
831 In: *Geological Records of Tsunamis and Other Extreme Waves*. Elsevier.
- 832 Valdovinos, C., Pedreros, P., 2007. Geographic variations in shell growth rates of the mussel
833 *Diplodon chilensis* from temperate lakes of Chile: Implications for biodiversity
834 conservation. *Limnologica* 37, 63–75.
- 835 Van Daele, M., Araya-Cornejo, C., Pille, T., Vanneste, K., Moernaut, J., Schmidt, S., Kempf, P.,
836 Meyer, I., Cisternas, M., 2019. Distinguishing intraplate from megathrust earthquakes using
837 lacustrine turbidites. *Geology* 47, 127–130.
- 838 Van Daele, M., Cnudde, V., Duyck, P., Pino, M., Urrutia, R., De Batist, M., 2014.
839 Multidirectional, synchronously-triggered seismo-turbidites and debrites revealed by X-ray

840 computed tomography (CT). *Sedimentology* 61, 861–880.

841 Villalobos, L., Parra, O., Grandjean, M., Jaque, E., Woelfl, S., Campos, H., 2003. A study of the
842 river basins and limnology of five humic lakes on Chiloé Island. *Revista Chilena de*
843 *Historia Natural* 76, 563-590.

844 Wesson, R.L., Melnick, D., Cisternas, M., Moreno, M., Ely, L.L., 2015. Vertical deformation
845 through a complete seismic cycle at Isla Santa Maria, Chile. *Nature Geoscience* 8, 547–551.

846